

Peculiar Velocity Reconstruction with Fast Action Method: Tests on Mock Redshift Surveys

Enzo Branchini¹, Amiram Eldar^{2,3} & Adi Nusser³

¹ *Dipartimento di Fisica, Università di Roma TRE, Via della Vasca Navale 84, 00146, Roma, Italy*

² *Racah Institute of Physics, The Hebrew University, Jerusalem 91904, Israel*

³ *Physics Department, Technion, Haifa 32000, Israel*

25 October 2018

ABSTRACT

We present extensive tests of the Fast Action Method (FAM) for recovering the past orbits of mass tracers in an expanding universe from their redshift-space coordinates at the present epoch. The tests focus on the reconstruction of present-day peculiar velocities using mock catalogs extracted from high resolution N -body simulations. The method allows for a self-consistent treatment of redshift-space distortions by direct minimization of a modified action for a cosmological gravitating system. When applied to ideal, volume limited catalogs, FAM recovers unbiased peculiar velocities with a 1-D, 1σ error of $\sim 220 \text{ Km s}^{-1}$, if velocities are smoothed on a scale of $5 \text{ h}^{-1}\text{Mpc}$. Alternatively, when no smoothing is applied, FAM predicts nearly unbiased velocities for objects residing outside the highest density regions. In this second case the 1σ error decreases to a level of $\sim 150 \text{ Km s}^{-1}$. The correlation properties of the peculiar velocity fields are also correctly recovered on scales larger than $5 \text{ h}^{-1}\text{Mpc}$. Similar results are obtained when FAM is applied to flux limited catalogs mimicking the IRAS PSCz survey. In this case FAM reconstructs peculiar velocities with similar intrinsic random errors, while velocity-velocity correlation properties are well reproduced beyond scales of $\sim 8 \text{ h}^{-1}\text{Mpc}$. We also show that FAM provides better velocity predictions than other, competing methods based on linear theory or Zel'dovich approximation. These results indicate that FAM can be successfully applied to presently available galaxy redshift surveys such as IRAS PSCz.

Key words: cosmology: theory – gravitation – dark matter – large scale structure of the Universe

1 INTRODUCTION

In the standard paradigm, the formation of cosmological structures is driven by gravitational amplification of tiny initial density fluctuations (e.g. Peebles 1980). In addition to gravity, hydrodynamical processes can greatly influence the formation and evolution of galaxies, groups and clusters of galaxies. Hydrodynamical effects, however, play a minor role in shaping the observed distribution of galaxies on scales a few times larger than the size of galaxy clusters. Therefore, gravitational instability theory directly relates the present-day large scale structure to the initial density field and provides the framework within which the observations are analyzed and interpreted. Gravitational instability is a non-linear process. Analytic solutions exist only for configurations with special symmetry, and approximate tools are limited to moderate density contrasts. So, numerical methods are necessary for a full understanding of the observed large scale structure of the universe. There are two complementary numerical approaches. The first approach relies on N -body techniques designed to solve an initial value problem in which the evolution of a self-gravitating system of massive particles is determined by numerical integration of the

Newtonian differential equations. Combined with semi-analytic models of galaxy formation, N -body simulations have become an essential tool for comparing the predictions of cosmological models with the observed properties of galaxies. Because the exact initial conditions are unknown, comparisons between simulations and observations are mainly concerned with general statistical properties. The second approach aims at finding the past orbits of mass tracers (galaxies) from their observed present-day distribution, independent as much as possible of the nature of the dark matter. The orbits must be such that the initial spatial distribution is homogeneous. This approach can be very useful for direct comparisons between different types of observations of the large scale structure. Most common are the velocity-velocity (hereafter v - v) comparisons between the observed peculiar velocities of galaxies and the velocity field inferred from the galaxy distribution in redshift surveys (Davis, Nusser & Willick 1996, Willick *et al.* 1997, Willick & Strauss 1998, Nusser *et al.* 2000, Branchini *et al.* 2001). Alternatively, one can also perform a density-density comparison between the mass density field inferred from the peculiar velocities of galaxies via POTENT-like methods (Bertschinger & Dekel 1989) or Wiener Filtering techniques (Zaroubi *et al.* 1995) and the observed galaxy distribution (see Sigad *et al.* 1998 and references therein). Both types of analysis yield the cosmological mass density parameter Ω_m , for an assumed biasing relation between the distribution of galaxies and the mass density field. Any systematic mismatch between the fields serves as an indication to the nature of galaxy formation and/or the origin of galaxy intrinsic scaling relations used to measure the distances, provided that errors in the calibration have been properly corrected for. This second approach also allows to perform back-in-time reconstructions of the density field on scales $\sim 5 \text{ h}^{-1} \text{ Mpc}$ both in real (e.g. Nusser & Dekel 1992, Gramman 1993, Croft & Gaztañaga 1998, Frisch *et al.* 2001) and redshift space (Narayanan & Weinberg 1998, Monaco & Efsthathiou 1999). Some of these methods has been applied to recover the past orbits from all-sky galaxy redshift surveys (Monaco *et al.* 2000, Narayanan *et al.* 2001).

Finding the orbits that satisfy initial homogeneity and match the present-day distribution of mass tracers is a boundary value problem. This problem naturally lends itself to an application of Hamilton's variational principle where the orbits of the objects are found by searching for stationary variations of the action subject to the boundary conditions. The use of the Principle of Least Action in a cosmological frame-work has been pioneered by Peebles (1989) and has long been restricted to small systems such as the Local Group (Peebles 1990, Peebles 1994, Schmoldt & Saha 1998, Sharpe *et al.* 2001) and the Local Supercluster (Shaya, Peebles & Tully 1995). Early applications to large galaxy redshift surveys have been hampered by the computational cost of handling the relatively large number of objects. Subsequent numerical applications speeded up the method and allowed the reconstruction of the orbits of $\sim 10^3$ particles (Shaya, Peebles & Tully 1995). However, it was only recently that the improvement of the minimization techniques and the use of efficient gravity solvers made it possible to deal with more than 10^4 objects (e.g. the Fast Action Method [hereafter FAM] by Nusser & Branchini 2000 and the Perturbative Least Action Method by Goldberg & Spergel 2000), comparable to the number of objects contained in the largest all-sky galaxy redshift catalogs presently available such as the Optical Redshift Survey (Santiago *et al.* 1995, 1996) and IRAS PSCz (hereafter PSCz, Saunders 1996, Saunders *et al.* 2000). The situation has also been improved thanks to the invention of self-consistent direct schemes for accounting for redshift distortions, arising from the systematic differences between the distribution of galaxies in real and redshift space (e.g. Kaiser 1987). Previous applications (e.g., Shaya, Peebles & Tully 1995) relied on iterations. However, self-consistent treatments of the problem have been proposed by Schmoldt & Saha (1998), Nusser & Branchini (2000), Phleps (2000), Susperregi (2001) and Goldberg (2001).

In this work we will implement and test one of the Numerical Action Methods on realistic large mock redshift catalogs to reconstruct galaxy orbits over a large region of the universe. More precisely we will extend the Fast Action Method of Nusser & Branchini (2000, hereafter NB) to redshift space and focus on the problem of predicting galaxy peculiar velocities from a flux-limited, all-sky redshift catalog resembling the PSCz one.

The outline of the paper is as follows. In Section 2 we review FAM in real and redshift space. The performance of FAM is evaluated in the case of the ideal spherical infall in Section 3. Then a suite of more demanding tests is performed using the mock catalogs of galaxies described in Section 4. FAM is then applied to ideal, volume-limited mock catalogs in Section 5 and to flux-limited mock catalogs in Section 6. Particular emphasis is given to the ability of FAM in returning an unbiased estimate of galaxy velocities and their correlation properties. The main conclusions are discussed and summarized in Section 7. We will use the terms FAMz and FAMr to refer to implementations of FAM in redshift and real distance space, respectively. Statements referring to FAM are meant to apply to both FAMz and FAMr. For brevity we will use x-space and s-space to refer to real-space and redshift-space, respectively.

2 THE FAST ACTION METHOD

In this Section we briefly summarize the Fast Action Method. For a detailed description of the method we refer the reader to Sections 2 and 4.2 of NB. We follow the standard notation in which $a(t)$ is the scale factor, $H(t) = \dot{a}/a$ is the Hubble function, $\Omega_m = \bar{\rho}/\rho_c$ is the ratio of the background matter density of the universe, $\bar{\rho}$, to the critical density, $\rho_c = 3H^2/8\pi G$.

We denote the comoving coordinate of a patch of matter by \mathbf{x} , and the corresponding comoving velocity by $\mathbf{v} = d\mathbf{x}/dt$. Also, let $D(t)$ be the linear density growing mode normalized to unity at the present epoch, and $f(\Omega_m) = d\ln D/d\ln a \approx \Omega_m^{0.6}$ (e.g., Peebles 1980). In the following we will use $D(t)$ as the time variable in the equations of motion, with $\boldsymbol{\theta} = d\mathbf{x}/dD$ as the corresponding velocity. Expressed in term of the time variable D , the equations of motion are almost independent on Ω_m and the cosmological constant (Gramann 1993, Mancinelli & Yahil 1995, Nusser & Colberg 1998).

The evolution of a cosmological self-gravitating, isolated system of N equal mass particles in a volume V is governed by the following equations of motion,

$$\frac{d\boldsymbol{\theta}_i}{dD} + \frac{3}{2} \frac{1}{D} \boldsymbol{\theta}_i = \frac{3}{2} \frac{1}{D^2} \frac{\Omega_m}{f^2(\Omega_m)} \mathbf{g}(\mathbf{x}_i), \quad (1)$$

where the subscript $i = 1 \cdots N$ is the particle index, and \mathbf{g} is the peculiar gravitational force field per unit mass. If the particles are unbiased tracers of the underlying density field then,

$$\mathbf{g}(\mathbf{x}) = -\frac{1}{4\pi\bar{n}} \sum_i \frac{\mathbf{x} - \mathbf{x}_i}{|\mathbf{x} - \mathbf{x}_i|^3} + \frac{1}{3} \mathbf{x}, \quad (2)$$

where $\bar{n} = N/V$ is the mean number density of particles inside V . In this expression for \mathbf{g} we have assumed that $NM = \bar{\rho}V$ where M is the mass of a particle. These equations of motion can be derived from the action,

$$S = \int_0^1 dD \sum_i \left\{ \frac{1}{2} D^{3/2} \boldsymbol{\theta}_i^2 + \frac{3}{2} \frac{1}{D^{1/2}} \frac{\Omega_m}{f^2(\Omega_m)} \left[\frac{1}{4\pi\bar{n}} \sum_{j<i} \frac{1}{|\mathbf{x}_i - \mathbf{x}_j|} + \frac{\mathbf{x}_i^2}{6} \right] \right\} \quad (3)$$

under stationary first variations of the orbits that leave \mathbf{x} fixed at the present epoch and satisfy the constraint $D^{3/2}\boldsymbol{\theta} \rightarrow 0$ as $D \rightarrow 0$ (Peebles 1989, NB). The second condition on the velocities guarantees homogeneity as $D \rightarrow 0$. FAMr expands the orbits in a time dependent base functions $q_n(D)$ in the form,

$$\mathbf{x}_i(D) = \mathbf{x}_{i,0} + \sum_{n=1}^{n_{max}} q_n(D) \mathbf{C}_{i,n}, \quad (4)$$

where $\mathbf{x}_{i,0}$ is the position of the particle i at the present epoch, and the vectors $\mathbf{C}_{i,n}$ are the expansion coefficients with respect to which the action is varied, i.e., they satisfy $\partial S/\partial \mathbf{C}_{i,n} = 0$. The base functions q_n and their derivatives $p_n(D) \equiv dq_n/dD$ are linear combinations of $(1-D)$, $(1-D)^2 \cdots (1-D)^{n_{max}}$ so that the particle positions at $D = 1$ is fixed, and $\lim_{D \rightarrow 0} D^{3/2} q_n(D) \boldsymbol{\theta}(D) = 0$ ensures initial homogeneity. To simplify the expression of the gradient of the action, $\partial S/\partial \mathbf{C}_{i,n}$, NB imposed following the orthonormality condition on the functions $p_n(D)$,

$$\int_0^1 dD D^{3/2} p_n(D) p_m(D) = \delta_{m,n}^K, \quad (5)$$

where δ^K is the Kronecker delta function. The expansion of the orbits given in (4) has to be modified when the constraints are galaxy redshifts, rather than the true distances. The redshift coordinate of an object is

$$\mathbf{s}_0 = H_0 \mathbf{x}_0 + (\mathbf{v}_0 \cdot \hat{\mathbf{s}}_0) \hat{\mathbf{s}}_0, \quad (6)$$

where the subscript 0 refers to quantities at the present time, and $\hat{\mathbf{s}}_0$ is a unit vector directed along the line of sight to the galaxy. When the constraints are the particle positions in s-space, $\mathbf{s}_{i,0}$, the appropriate expansion of the orbits can be written as,

$$\mathbf{x}_i(D) = H_0^{-1} \mathbf{s}_{i,0} + \sum_n q_n(D) \mathbf{C}_{i,n} - f_0 \left(\sum_n p_{n,0} \mathbf{C}_{i,n}^{\parallel} \right) \hat{\mathbf{s}}_{i,0}, \quad (7)$$

where $p_{n,0} = p_n(D = 1)$, and the symbol (\parallel) indicates the component of a vector in the direction of line of sight at the present epoch, $\hat{\mathbf{s}}_{i,0}$. The trivial dependence on H_0 can be completely eliminated by working with $H_0 \mathbf{x}$ instead of \mathbf{x} . With this expression for the orbits, the gradient of the action subject to the new boundary conditions is

$$\partial S/\partial \mathbf{C}_{i,n} = \mathbf{I}_{i,n} - f_0 p_{n,0} \left(\boldsymbol{\theta}_{i,0}^{\parallel} + \mathbf{I}_{i,n}^{\parallel} \right), \quad (8)$$

where $f_0 = f(\Omega_{m,0})$,

$$\mathbf{I}_{i,n} = \int_0^1 dD D^{3/2} q_n \left[\frac{d\boldsymbol{\theta}_i}{dD} + \frac{3}{2} \frac{\boldsymbol{\theta}_i}{D} - \frac{3}{2} \frac{1}{D^2} \frac{\Omega_m}{f^2} \mathbf{g}_i \right] \quad (9)$$

and

$$\mathbf{I}_{i,n}^{\parallel} = \int_0^1 dD D^{3/2} q_n \left[\frac{d\boldsymbol{\theta}_i^{\parallel}}{dD} + \frac{3}{2} \frac{\boldsymbol{\theta}_i^{\parallel}}{D} - \frac{3}{2} \frac{1}{D^2} \frac{\Omega_m}{f^2} \mathbf{g}_i^{\parallel} \right]. \quad (10)$$

The equations (8) differ from the equations of motion by the boundary term, $f_0 p_{n,0} \left(\boldsymbol{\theta}_{i,0}^{\parallel} + \mathbf{I}_{i,n}^{\parallel} \right)$. This term can be eliminated by adding a kinetic energy term to the action, as follows

$$\mathcal{S} = S + \frac{1}{2} f_0 \sum_i \left(\boldsymbol{\theta}_{i,0}^{\parallel} \right)^2. \quad (11)$$

Given the redshifts of the particles, the minimization of the action \mathcal{S} leads to the equations of motions (eq. 1). Similar transformations of this type have been proposed by Schmoldt & Saha (1998) and Withering (2001).

Our strategy is to find orbits that are as close as possible to the Hubble flow. Therefore, we search for the minimum of the action and do not look for stationary points which might describe oscillatory behavior of the orbits (Peebles 1990, 1994). To find the coefficients $\mathbf{C}_{i,n}$ that minimize the action, FAM uses the Conjugate Gradient Method (CGM) which is fast and easy to implement (Press *et al.* 1992). The gravitational force \mathbf{g} and its potential are computed using the TREECODE gravity solver (Bouchet & Hernquist 1988). The time integration in the expression for the action is done using the Gaussian quadrature method with 10 points at the time abscissa (Press *et al.* 1992). The CGM requires an initial guess for $\mathbf{C}_{i,n}$. In the standard FAM application we compute the initial guess using the linear theory relation between the velocity and mass distribution. The minimum of the action proved to be rather insensitive to the choice of initial guess for $\mathbf{C}_{i,n}$, as we have checked by running FAM experiments with initial $\mathbf{C}_{i,n}$ both set to zero and to random numbers with appropriate variance. Besides the initial set of $\mathbf{C}_{i,n}$, the other free parameters are the softening used by the gravity solver and the tolerance parameter that sets the convergence of the CGM method.

3 THE SPHERICAL INFALL MODEL TEST

The collapse of a spherical over-dense perturbation can be followed analytically into the nonlinear regime before the occurrence of shell crossing (e.g., Peebles 1980). Testing FAM with the spherical collapse model will allow an assessment of the “shot-noise” errors in the recovered velocities. These errors arise from the discrete sampling of the density field and can be quantified by applying FAM in two different ways. In the first, we treat each particle as a uniform spherical shell. So the gravitational field on a particle is radial and only due to particles lying within its radius. In this way particles move along radial orbits and shot-noise errors are minimized. In the second, each particle is treated as point mass and the gravitational field is computed from the TREECODE as in any other application of FAM. The comparison between the peculiar velocities in these two different ways of applying FAM is an important test for assessing the performance of FAM under general conditions.

Consider a spherical density fluctuation described by the following radial density profile at the initial redshift $z_{in} = 50$:

$$\delta_{in}(r) = \delta_0 \left[1 + \left(\frac{r}{r_c} \right)^2 \right]^{-3}, \quad (12)$$

where $r_c = 40(1 + z_{in})^{-1}$ Mpc, $\delta_0 = (1 + z_{in})^{-1}$. The corresponding initial velocity is obtained using the velocity-density relation of the linear growing mode. We assume a flat universe with $\Omega_m = 1$ and $\Omega_\Lambda = 0$. The analytic solution returns the density and peculiar velocity fields at a generic time. The evolved density field is then randomly sampled with 20,000 particles within 80 Mpc. Each particle is then assigned a peculiar velocity according to the analytic solution and its redshift coordinate is computed accordingly. The distribution of these particles in x-space and s-space are then fed into FAMr and FAMz, respectively. We have used $n_{max} = 6$ base functions to expand the orbit of each particle, a softening of $\epsilon = 0.5$ Mpc, and a tolerance parameter $tol = 10^{-8}$ to determine the convergence of the CGM solution.

In the first FAM experiments, particles move in radial orbits under the action of the radial gravity force. The final radial velocity profiles in the FAMr and FAMz experiments are shown, respectively, in the top-left and top-right panels of fig. 1.

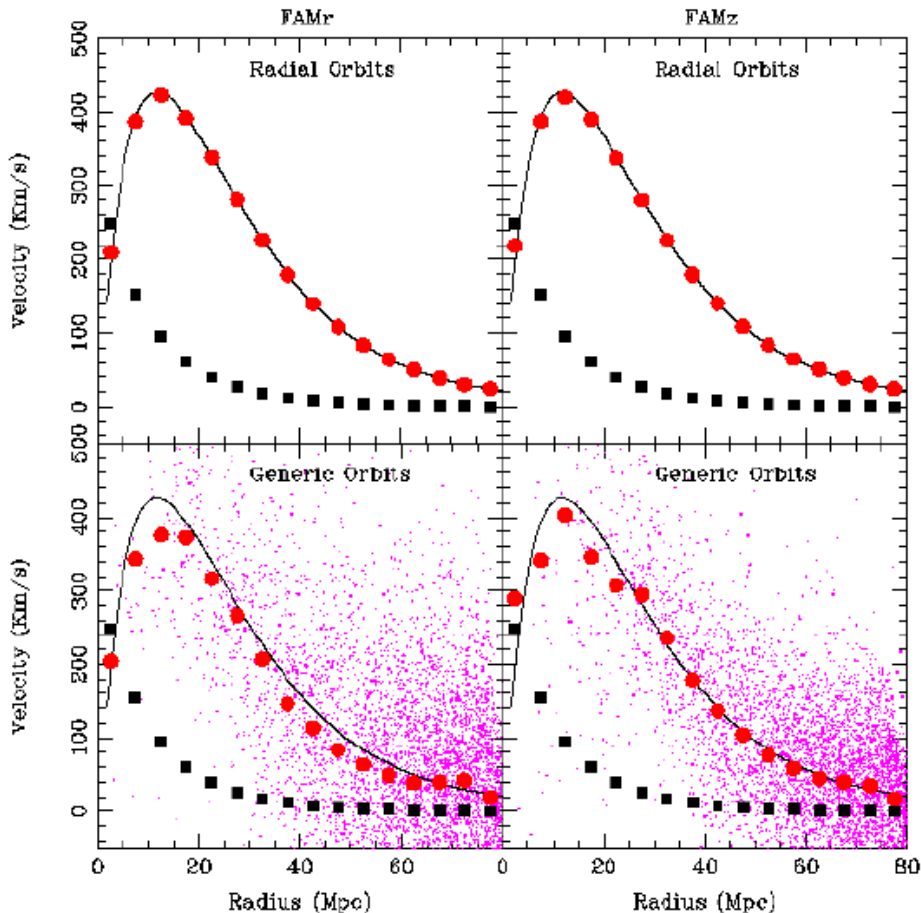


Figure 1. Radial velocity profiles from FAMr (left) and FAMz (right) experiments. In all panels the continuous line shows the analytic solution for the spherical infall case. Filled dots represent the average FAM radial velocities measured in radial shells of 5 Mpc. The filled squares show the final overdensity profile, $\delta_{fin}(r) \times 100$. The numerical solution shown in the top panels is obtained by imposing radial FAM orbits. This constraint is removed in the solutions shown in the two bottom plots, where the scattered points represent FAM radial velocities measured at the position of a subset of particles.

In both panels, the velocity profile in the analytic solution is represented by the continuous solid line. The filled dots show the average peculiar velocity computed within radial shells of 5 Mpc. The scatter around the mean is negligible. The filled squares represent the final overdensity profile, $\delta_{fin}(r) \times 100$, also in radial bins of 5 Mpc. Both FAMr and FAMz match the analytic solution very well at all radii.

We have repeated the FAMz and FAMr experiments with the gravity force field computed by summing over the 3-dimensional discrete distribution of the point masses. This generates random shot-noise errors in the FAM recovered velocities. The radial velocity profiles are shown in the two bottom panels of fig. 1. The results of the FAMr and FAMz experiments are very similar. The average FAM solutions (filled dots) are still close to the true one. FAM appears to underestimate the true velocities in the high density regions. However, the effect is of little significance ($\sim 30 \text{ Km s}^{-1}$) when compared to the 1-D scatter around the mean ($\sim 120 \text{ Km s}^{-1}$) which, instead, does not seem to depend on the local density.

The amplitude of the random errors is better appreciated in fig. 2, where we plot the Cartesian X-component of true *vs.* FAM velocities of ~ 1000 randomly selected particles. The parameters of the best linear fit and its 1-D, 1σ scatter are shown in each panel. The diagonal line in each panel is plotted to guide the eye. The two upper panels show the results when the particles are forced to move along radial orbits. When this constraint is removed (lower panels), the shot noise error causes a $120 - 150 \text{ Km s}^{-1}$ uncertainty in FAM reconstructions which is clearly visible both in x- (bottom-left) and s-space (bottom-right). The small systematic errors seen in fig. 1 are also visible in fig. 2 and cause the FAM velocities to be slightly underestimated, especially when the reconstruction is performed in x-space. Systematic errors can be quantified by the deviation of the slope of the best fitting line from unity. The main source for the systematic mismatch is the softening used in the TREECODE to compute the force field. As already pointed out by NB, the amplitude of FAM velocities decreases

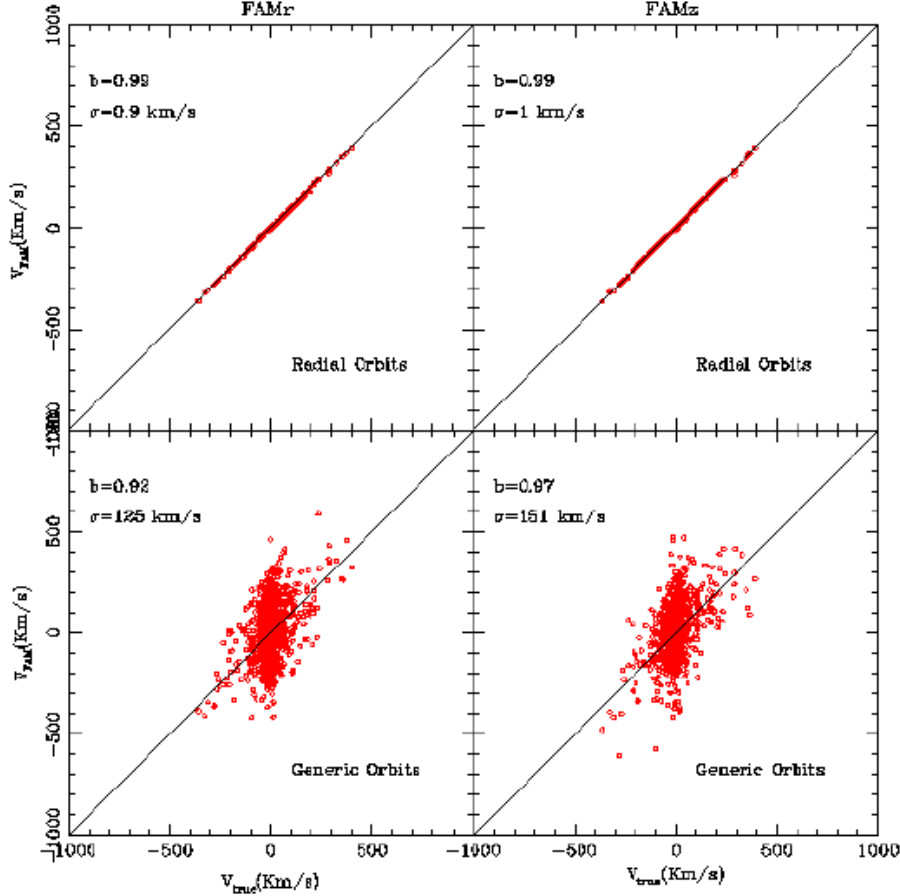


Figure 2. Cartesian X-components of FAMr (left) and FAMz (right) velocities vs. true ones. Only velocities of ~ 1000 randomly selected particles are shown. The upper panels show the case of purely radial orbits. The lower panels show the case of unconstrained orbits. The results of the least square fit and the 1-D, 1σ scatter around the best fitting line are indicated in each panel.

when increasing the softening parameter, along with the scatter around the best fitting line. This is true also in the spherical infall experiment, as we have checked by running the same FAMr with a smaller softening parameter of $\epsilon = 0.25$ Mpc. As expected, using a smaller softening reduces systematic errors and increases the slope of the best fitting line from 0.92 to 0.95.

We have also tested FAMz with spherical infall in a universe with $\Omega_m = 0.3$ and $\Omega_\Lambda = 0.7$. FAMz velocities are still free of systematic biases and the relative random errors are similar to those found in the previous tests in a flat, $\Omega_m = 1$ universe.

4 THE MOCK N -BODY CATALOGS

In Sections 5 and 6 we will perform more realistic and demanding tests of FAM using a suite of mock catalogs extracted from two N -body simulations performed by Cole *et al.* (1998). The initial conditions of the two simulations were generated, respectively, from two cosmological models of Cold Dark Matter: a flat Λ CDM model with $\Omega_m = 0.3$ and $\Omega_\Lambda = 0.7$, and a flat τ CDM universe with $\Omega_m = 1.0$ and power spectrum shape parameter $\Gamma = 0.25$. Both simulations were ran with an AP³M code loaded with 192^3 particles in a box of side $345.6 h^{-1}$ Mpc. In both simulations the initial amplitude of the density fluctuations was normalized to the observed abundance of galaxy clusters. This requires setting $\sigma_8 = 0.55\Omega_m^{-0.6}$ (Eke, Cole & Frenk 1996), where σ_8 is the linear rms mass density fluctuation in top-hat spheres of radius $8 h^{-1}$ Mpc (which hereafter we indicate with TH8). Before generating the mock catalogs the distribution of N -body particles has been re-sampled by assigning a constant probability to each particle which is used to perform a Montecarlo rejection procedure from a Poisson distribution with mean equal to the required probability. The original N -body particles are thus substituted by 0,1,2 or on rare occasions an even higher number of particles that retain positions and velocities of the parent object. Particles at the same locations are usually collapsed into a single objects with higher mass. Occasionally, however, roundoff errors cause

Table 1. Main properties of the four sets of mock catalogs. Name: Label of the set. $\#_{Cat}$: Number of catalogs in each set (representative of Λ CDM and τ CDM cosmological models). $\#_{Part}$: Number of particles in each catalog. Sampling: Monte Carlo sampling technique adopted. R_{TH} : radius of the top-hat filter used to smooth the original simulation (l represents the average interparticle separation). R_{max} : external radius of each sample.

Name	$\#_{Cat}$	$\#_{Part}$	Sampling	R_{TH} (h^{-1} Mpc)	R_{max} (h^{-1} Mpc)
VL	5+5	20000	10000+10000	0	80
VL5TH	5+5	20000	10000+10000	5	80
FL	5+5	~ 8000	PSCz Selection	0	80
FL5TH	5+5	~ 8000	PSCz Selection	Max [5, l]	80

them to be retained as close pairs or triplets of particles. Furthermore, we have cooled down the particles' peculiar velocities since they are significantly larger than those of real galaxies. The new peculiar velocities \mathbf{v} are obtained in two steps (Davis, Nusser & Willick 1996). First we perform a mass-weighted smoothing of the N -body velocities, \mathbf{v}_{Nbody} , with a spherical top hat filter of radius $1.5 h^{-1}$ Mpc and obtain a smoothed velocity field $\mathbf{v}_{1.5}$. Then the two vector fields are added linearly to give $\mathbf{v} = 0.7 \times \mathbf{v}_{Nbody} + 0.3 \times \mathbf{v}_{1.5}$. The new pairwise velocity dispersion measured for object with a relative separation of $1.0 h^{-1}$ Mpc is $\sim 200 \text{ Kms}^{-1}$, comparable to the value measured by Strauss, Ostriker & Cen (1998) for galaxies outside high density region in the Optical Redshift Survey.

From these two simulations we have extracted 4 sets of mock catalogs. Each catalog lists particle positions, redshifts, and peculiar velocities in a spherical region of radius of $80 h^{-1}$ Mpc centered on a Local-Group look-alike particle (see Branchini *et al.* 1999 for details). Each set contains 5+5 independent mock catalogs, corresponding to the two simulations, so that in total we have 40 catalogs. The four sets are termed VL, VL5TH, FL, and FL5TH and their main properties are summarized in table 1. The sets VL and VL5TH are volume-limited catalogs, while FL and FL5TH are flux-limited.

A catalog in the VL set is generated by randomly extracting 20,000 particles in a sphere of radius $80 h^{-1}$ Mpc, half of which sample the inner sphere of radius $40 h^{-1}$ Mpc and the rest are contained in the shell between 40 and $80 h^{-1}$ Mpc. Different masses have been assigned to internal and external particles to guarantee the same average mass density throughout the volume. A typical VL mock catalog is displayed in the top-left panel of fig. 3 which shows a slice of thickness $20 h^{-1}$ Mpc cut through a VL mock catalog extracted from the τ CDM simulation.

To obtain the VL5TH catalogs we first smooth in x -space the particles' distribution in the N -body simulation in a mass-weighted fashion with a spherical top-hat filter of radius $5 h^{-1}$ Mpc and then we Poisson sample the smoothed density field with 20,000 particles, half of which inside $40 h^{-1}$ Mpc. The bottom-left panel of fig. 3 shows the x -space particle distribution in one of the VL5TH catalogs. The particle distribution appears to be less clustered than in the unsmoothed case, as expected. The redshifts of mock galaxies are obtained by adding the radial component of the 5TH-smoothed N -body velocities to the particles' distance (expressed in Kms^{-1}).

The sets FL and FL5TH are designed to mimic the PSCz flux-limited survey. A FL mock catalog typically contains ~ 8000 particles within a sphere of $80 h^{-1}$ Mpc, extracted from the N -body simulation according to the selection function of PSCz galaxies as determined by Branchini *et al.* (1999):

$$\phi(r) = \begin{cases} 1 & \text{if } r \leq 6 h^{-1}\text{Mpc} \\ \left(\frac{r}{r_0}\right)^{-1.08} \left(1 + \frac{r^2}{r_*^2}\right)^{-1.83} & \text{if } r > 6 h^{-1}\text{Mpc} \end{cases} \quad (13)$$

where r is the distance from the center of the sphere in h^{-1} Mpc, $r_0 = 6.05 h^{-1}$ Mpc, and $r_* = 87 h^{-1}$ Mpc. The mass assigned to each galaxy is equal to the inverse of the selection function at the galaxy position $\phi(\mathbf{x})$. An example of catalog in the FL set is shown in the top-right panel of fig. 3. The particle distribution is concentrated towards the center due to the cut in flux. To obtain the FL5TH catalogs we follow a two step procedures. First we perform a mass-weighted smoothing of the particle distribution in the x -space within each of the FL mock catalogs using a top-hat filter with an adaptive radius of $R_{TH} = \text{Max}[5, l] h^{-1}$ Mpc, where l is the average inter-particle separation at the generic position. This smoothing radius compromises the need of avoiding nonlinear effects with that of minimizing shot noise errors. Then we sample the smoothed density with ~ 8000 particles with a radial distribution according to the selection function (eq. 13). The particle distribution in one of the FL5TH mock catalogs is shown in the bottom-right panel of fig. 3. As for the VL5TH case, the redshifts of the mock galaxies in the FL5TH catalogs are obtained using the velocities smoothed with a top hat filter on the variable scale R_{TH} .

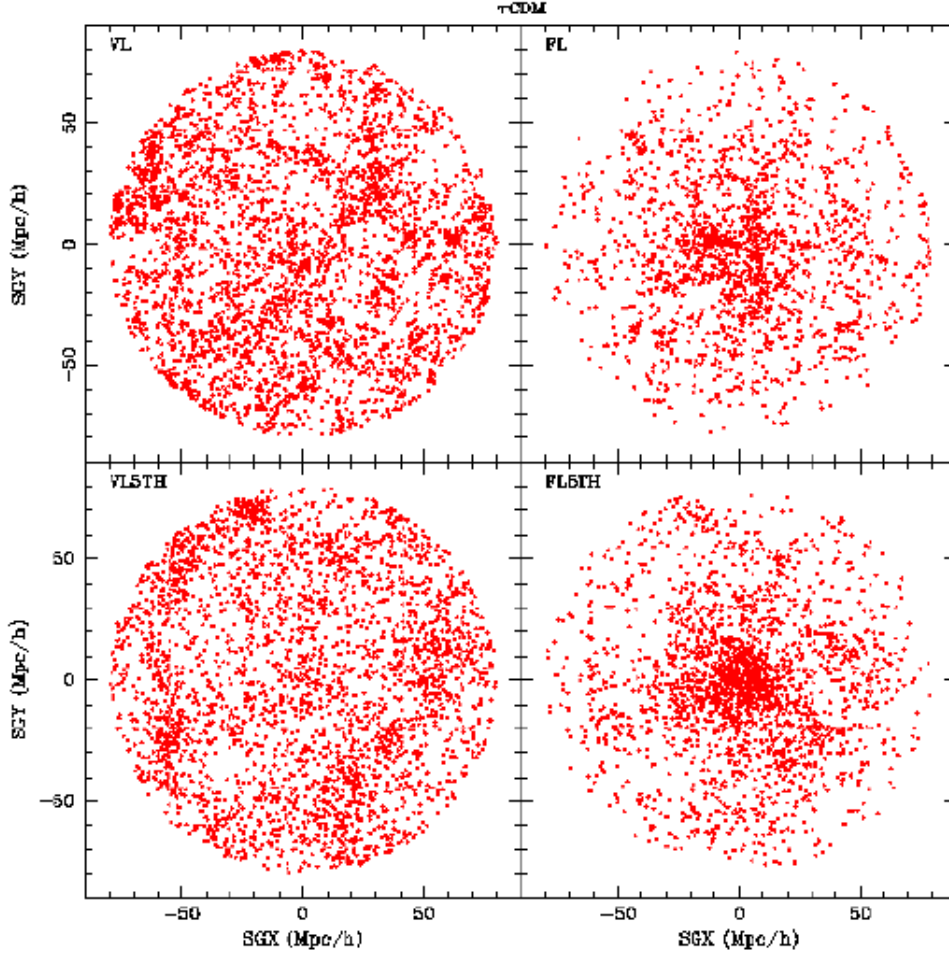


Figure 3. Particle distribution in x-space in slices of thickness $20 h^{-1} \text{Mpc}$ cut through mock catalogs in the τCDM N -body simulation. Each panel shows a VL (top-left), VL5TH (bottom-left), FL (top-right), and FL5TH (bottom-right) mock catalog selected from the 4 sets.

5 TESTS WITH VOLUME-LIMITED CATALOGS

In this Section we apply FAM to the suite of VL and VL5TH catalogs. Unless otherwise stated, all FAM reconstructions were performed with a softening $\epsilon = 0.5 h^{-1} \text{Mpc}$, a tolerance $tol = 10^{-6}$, and $n_{max} = 6$ basis functions. Decreasing tol or increasing n_{max} makes little change to the final results.

5.1 Unsmoothed Volume-Limited: VL

In fig. 4 we show maps of the N -body and FAMz peculiar velocities for one of the VL catalogs. The vectors represent the 2D-projected peculiar velocities of particles in a slice of thickness $6 h^{-1} \text{Mpc}$ cut through one of the VL- τCDM catalogs. The length of the vectors is drawn in units of $1 h^{-1} \text{Mpc} = 50 \text{Kms}^{-1}$. The top-left panel shows FAMz velocities for all the particles in the slice. The N -body velocities of the same particles are shown in the middle-left panel, and the velocity residuals, $\mathbf{v}_{Nbody} - \mathbf{v}_{FAMz}$, in the the bottom-left. Points with the largest residuals are located in regions of high density. These regions are characterized by virial velocities which are not modeled correctly by FAM. In these regions, FAM typically predicts a large, coherent infall into the gravitational potential wells of density peaks. One example is the region centered around the point with $(\text{SGX}, \text{SGY}) \approx (60, 0)$. The signature of virial motions is clearly visible in the N -body velocity map but is completely absent in FAM. Instead, FAM predicts coherent inward streaming velocities.

FAM is meant to model gravitational dynamics in the mildly nonlinear regime. So when we move away from high density environments we expect an improvement in the agreement between the N -body and FAM velocities. To verify this hypothesis, we define δ_5 as the density contrast smoothed with a TH5 filter and we only compare velocities of particles in regions with δ_5

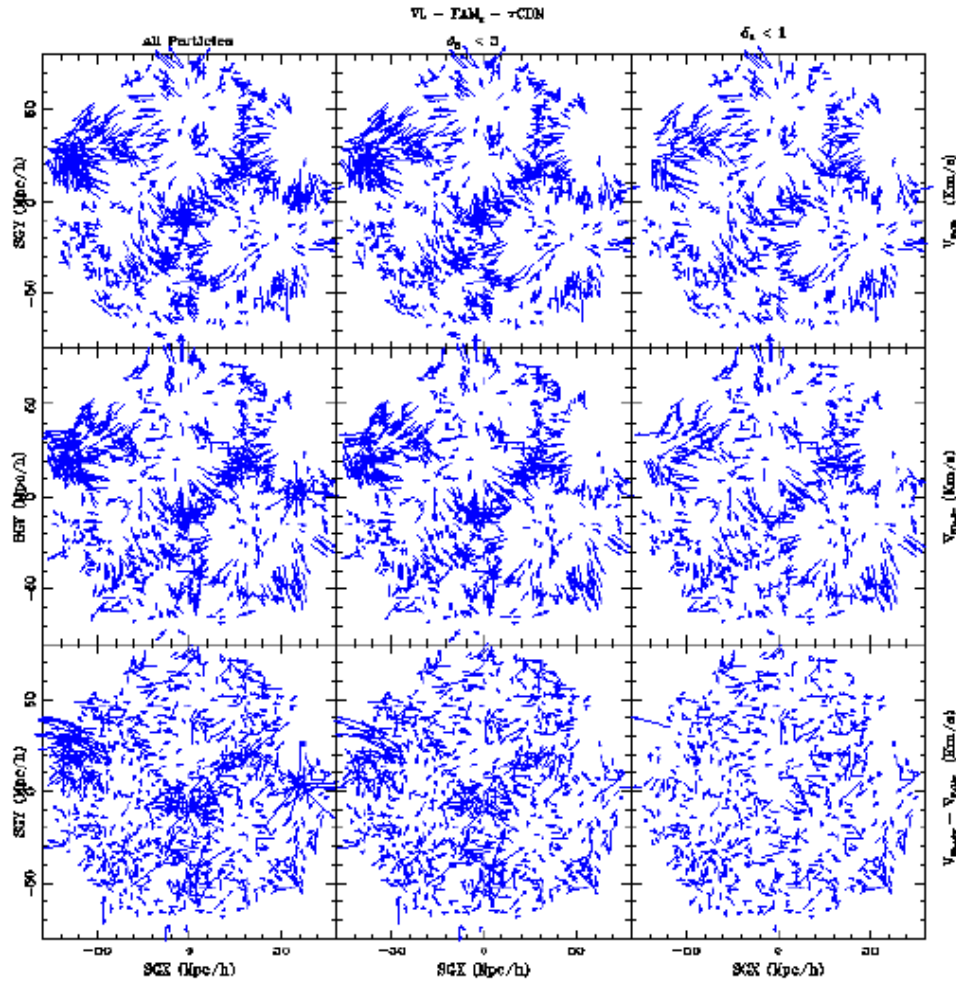


Figure 4. Maps of 2D-projected peculiar velocities for points residing in a slice of thickness $6 h^{-1}\text{Mpc}$ cut through a VL- τCDM catalog. The length of the vectors is drawn in units of $1 h^{-1}\text{Mpc} = 50 \text{Kms}^{-1}$. The top row shows the FAMz-predicted velocities. N -body velocities are shown in the middle row. The velocity residuals, $\mathbf{v}_{Nbody} - \mathbf{v}_{FAMz}$, are displayed on the bottom. The maps shown in the panels to the left hand side refer to all the points in the slice while only the velocities of points with $\delta_5 < 3$ and $\delta_5 < 1$ are plotted in the central and right columns, respectively.

less than a certain value. The central column of fig. 4 shows peculiar velocities of particles in regions with $\delta_5 < 3$. Cutting at this density threshold excludes only $\sim 5\%$ of the particles, but considerably improves the agreement between the two fields (the “hot spot” located at $(\text{SGX}, \text{SGY}) \approx (60, 0)$ disappears from the map of the residuals). The agreement further improves when we exclude points in regions with $\delta_5 \geq 1$ ($\sim 20\%$ of the points), as shown by the third row of panels in fig. 4. In this last case the velocity residuals (bottom-right) are further reduced and are not concentrated around regions of enhanced density. Very few large residuals still exist for points with large N -body velocities.

Fig. 5 shows a more quantitative point by point $v-v$ comparison. In each panel the Cartesian X-components of the N -body velocities is plotted against the corresponding FAMz (top panels) and FAMr (bottom panels) peculiar velocities. Each panel shows the velocities of 500 particles randomly selected from the total of 50,000 lying within a distance of $40 h^{-1}\text{Mpc}$ in all the 5 VL- τCDM catalogs. The left column shows the velocities of all particles. The panels in the middle and right columns show only the velocities of particles with $\delta_5 < 3$ and $\delta_5 < 1$, respectively.

To quantify the match between FAM and N -body velocities we perform a linear regression of the X-Cartesian components of N -body velocities on FAM assuming errors on the N -body velocities only, using all the particles 50,000 in the 5 VL- τCDM catalogs. The average slope and 1-D scatter of the regression of the 5 catalogs in each set are shown in the corresponding panels of fig. 5 along with the rms values of the average slope and 1-D velocity scatter over the 5 catalogs. The reasoning behind performing the linear regression of N -body velocities on FAM with errors on the N -body velocities is twofold. First, as pointed out by Berlind, Narayanan and Weinberg (2000), N -body velocities consist of a large-scale contribution predicted from the mass distribution plus an uncorrelated small-scale contribution that can be regarded as a thermal noise. This suggests putting all the errors on the N -body velocities, while leaving the FAM-reconstructed velocities on the X-axis. Second, this

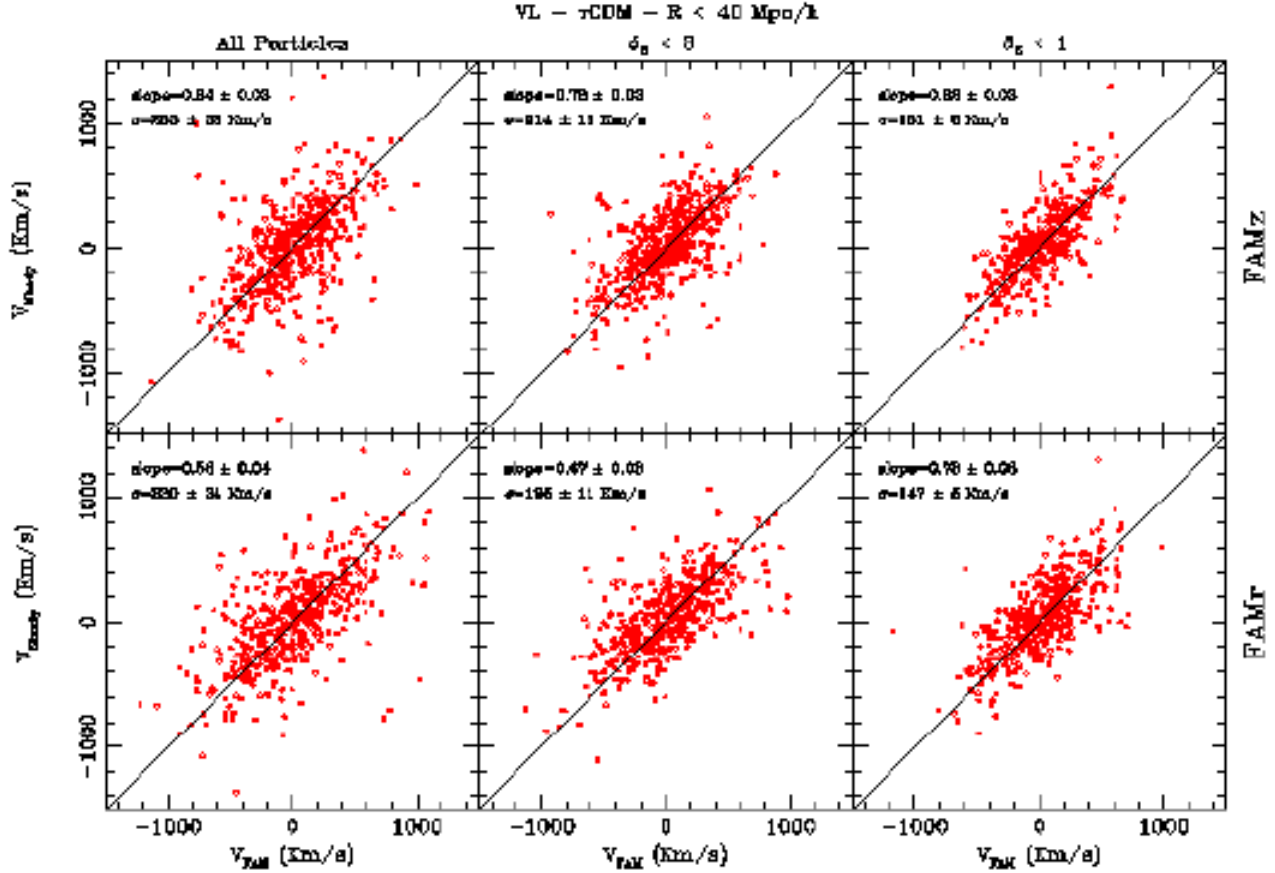


Figure 5. N -body vs. FAM particle velocity scatter plots in x -space (bottom panels) and s -space (top panels). Only the X -Cartesian velocity component of 500 objects, randomly selected among the 50,000 contained within $40 \text{ h}^{-1}\text{Mpc}$ from the center of the 5 VL - τ CDM catalogs are plotted. Particles in the left panels are selected from all density environments while only particles with $\delta_5 < 3$ and $\delta_5 < 1$ are displayed in the central and right panels, respectively. In all the plots, we show the slope and the 1-D velocity scatter around the fit (which uses all the 50,000 objects available) while the straight line shows the expected correlation.

choice mimics the real velocity-velocity comparisons in which the observed (N -body) velocities are compared with theoretical (FAM) predictions and the regression is performed putting all the errors in the observed quantity.

The top and bottom panels on the left hand side of fig. 5 show a clear correlation between N -body and FAM velocities with small scatter around the best fitting line, both in x - and s -space, although in both cases FAM overestimates the amplitude of the velocities. A few out-liers are present in the plots. However, while FAMz (top-left) underestimates the amplitude of the velocities of the out-liers, FAMr (bottom-left) does the opposite. So the slopes of the linear fits in FAMr are smaller than the corresponding slopes in FAMz. When the comparison is restricted to particles with $\delta_5 < 3$ (central row) the number of out-liers decreases and the agreement with N -body velocities improves significantly, indicating that discrepant velocities arise in high density regions as suggested by the velocity maps in fig. 4. This trend is confirmed by the scatter plots on the right column which only include points with $\delta_5 < 1$, well outside high density environments. In this last case the slopes of the FAMr and FAMz best fits are quite similar and even closer to unity. Furthermore, the out-liers have almost disappeared and the 1-D velocity scatter around the fit decreased to a very small level of $\approx 150 \text{ Kms}^{-1}$, to be compared with a typical 1-D rms velocity dispersion of $\approx 350 \text{ Kms}^{-1}$ for the objects in the VL catalogs. We conclude that FAMz and FAMr perform similarly outside high density regions (i.e. for $\sim 95\%$ of the points). The results of the fits shown in the plots are summarized in the upper part of table 2. The column labeled by 4σ , indicates the result of linear regressions in which out-liers in the v - v scatter plots are eliminated by iteratively discarding all points deviating by more than 4σ from the best fitting line. The 4σ -clipping procedure converges in a few iterations. The final outcome of this procedure is similar to that of imposing a density cut at $\delta_5 = 1$ and returns a best fit closer to unity.

So far only particles within $40 \text{ h}^{-1}\text{Mpc}$ were included in the v - v comparisons, although all particles out to $80 \text{ h}^{-1}\text{Mpc}$

Table 2. FAMr and FAMz results for the VL (upper part) and FL (lower part) experiments for two different cosmological models (τ CDM and Λ CDM). The average slope, b , and 1-D velocity scatter σ (in Km s^{-1}) are shown along with their rms scatter, measured over the 5 independent experiments. The best fit values are listed for various overdensity thresholds δ_5 and for the case of 4σ -clipping.

Model	FAMr				FAMz			
	All	$\delta_5 < 3$	$\delta_5 < 1$	4σ	All	$\delta_5 < 3$	$\delta_5 < 1$	4σ
VL- τ CDM	b 0.58 ± 0.04	0.67 ± 0.03	0.78 ± 0.03	0.80 ± 0.03	0.64 ± 0.03	0.78 ± 0.03	0.82 ± 0.03	0.82 ± 0.04
	σ 230 ± 24	195 ± 11	147 ± 5	131 ± 5	253 ± 33	214 ± 15	161 ± 8	141 ± 8
VL- Λ CDM	b 0.43 ± 0.03	0.71 ± 0.03	0.84 ± 0.04	0.88 ± 0.03	0.68 ± 0.02	0.82 ± 0.03	0.86 ± 0.04	0.91 ± 0.06
	σ 287 ± 55	161 ± 12	124 ± 7	105 ± 10	295 ± 59	167 ± 12	126 ± 6	108 ± 6
FL- τ CDM	b 0.67 ± 0.03	0.72 ± 0.03	0.78 ± 0.02	0.81 ± 0.03	0.74 ± 0.04	0.80 ± 0.04	0.88 ± 0.03	0.92 ± 0.05
	σ 227 ± 12	201 ± 10	171 ± 12	152 ± 14	242 ± 16	212 ± 14	170 ± 13	145 ± 12
FL- Λ CDM	b 0.51 ± 0.02	0.70 ± 0.03	0.86 ± 0.03	0.94 ± 0.03	0.67 ± 0.06	0.86 ± 0.04	0.93 ± 0.02	0.96 ± 0.03
	σ 223 ± 26	168 ± 24	135 ± 14	108 ± 9	240 ± 60	164 ± 24	126 ± 15	99 ± 11

were used in FAM reconstruction. This is to guarantee dense sampling (the outer part of these catalogs is more sparsely sampled) and to minimize the effect of the external tidal field. Including all particles out to $80 \text{ h}^{-1}\text{Mpc}$ does not affect the result appreciably, apart from a systematic $\sim 5\%$ increase in the slope of the best fitting line, which probably quantifies the bias introduced by having assumed a homogeneous mass distribution beyond $40 \text{ h}^{-1}\text{Mpc}$ in the former experiments. Similar considerations apply to the softening parameter. While, as shown in the NB analysis, increasing the softening parameter decreases the amplitude of FAM velocities, decreasing it from 0.5 to $0.25 \text{ h}^{-1}\text{Mpc}$ leaves the results of the v - v comparison unchanged.

We have also checked the dependence of our results on the cosmological model by repeating the same analysis with the 5 VL catalogs extracted from the Λ CDM N -body experiment. The parameters of the linear fits to the v - v comparisons are also listed in table 2 and are similar to those found in the τ CDM scenario. As for the τ CDM case, FAMr velocities are systematically larger than the FAMz ones and the mismatch with N -body velocities decreases when moving away from high density regions. The effect is more dramatic in the Λ CDM universe, as it can be verified by comparing the results of the fits with no density cut with those of the $\delta_5 = 3$ cut. The reason for this behavior is that the Λ CDM model is characterized by a larger value of σ_8 , i.e. by a larger number of regions with high overdensity where FAM fails to predict the correct peculiar velocities.

The v - v scatter plots tell us little about the ability of FAM at recovering the correlation properties of the velocity field. These have been investigated using two different statistical tools. The first is the average relative pairwise velocity $\langle V_{12} \rangle \equiv \langle [\mathbf{v}(\mathbf{x} + \mathbf{r}_{12}) - \mathbf{v}(\mathbf{x})] \cdot \mathbf{e}_{12} \rangle$, where the averaging is over all pairs of objects at separation $|\mathbf{r}_{12}|$, and \mathbf{e}_{12} is a unit vector along the the separation defined so that approaching pairs have $\langle V_{12} \rangle > 0$. The second statistics is the v - v correlation function projected along \mathbf{r}_{12} , defined as $\langle V_1 V_2 \rangle \equiv \langle \mathbf{v}(\mathbf{x}) \cdot \mathbf{e}_{12} \mathbf{v}(\mathbf{x} + \mathbf{r}_{12}) \cdot \mathbf{e}_{12} \rangle$ (Gorski 1988). These statistics have been computed for each of the VL catalogs. The results are shown in fig. 6 for the τ CDM case. Each ‘‘ribbon’’ represents the 1σ uncertainty interval around the mean values of $\langle V_{12} \rangle$ and $\langle V_1 V_2 \rangle$, averaged over the 5 reconstructions and plotted as a function of $|\mathbf{r}_{12}|$. The vertically-dashed and horizontally-dashed strips show the results of the FAMz and FAMr experiment. The dark strips show the ‘‘true’’ statistics computed from the N -body velocities. Similarly to fig. 6, the two plots to the right have been obtained using all the particles within $75 \text{ h}^{-1}\text{Mpc}$ while only particles with $\delta_5 < 3$ and $\delta_5 < 1$ have been used in the two other plots.

The top-left panel shows that at separations smaller than $\sim 1 \text{ h}^{-1}\text{Mpc}$, both $\langle V_{12} \rangle_x$ and $\langle V_{12} \rangle_s$ are systematically larger than the N -body result. This is the signature of what we have already spotted in the velocity maps, i.e. that in high density region (where most of the pairs with small relative separation reside) FAM predicts coherent infall ($\langle V_{12} \rangle > 0$) instead of disordered thermal motions ($\langle V_{12} \rangle = 0$). Also, the FAMr-predicted infall velocities are larger than the FAMz ones at separation smaller than few Megaparsecs. As we have already noticed in the linear fit to the v - v comparisons, this systematic discrepancy is caused by the smearing of density peaks in s -space which decrease the number of pairs having one member in over-dense regions and suppress the infall signal in the FAMz reconstructions. The same considerations apply to the plot on the bottom-left corner, which shows that the spurious infall makes $\langle V_1 V_2 \rangle$ of FAM velocities systematically smaller than the N -body one up to scales of $\sim 3 \text{ h}^{-1}\text{Mpc}$. These considerations are verified by the middle and right columns of fig. 6. Removing the high density regions does not change significantly the FAM average results but only the scatter. In contrast, the N -body results change appreciably, especially at small separations. This indicates that most of the infall signal in the FAM velocities comes from close pairs (since the solution of first approach is the one preferentially found at the minimum of the action) which do

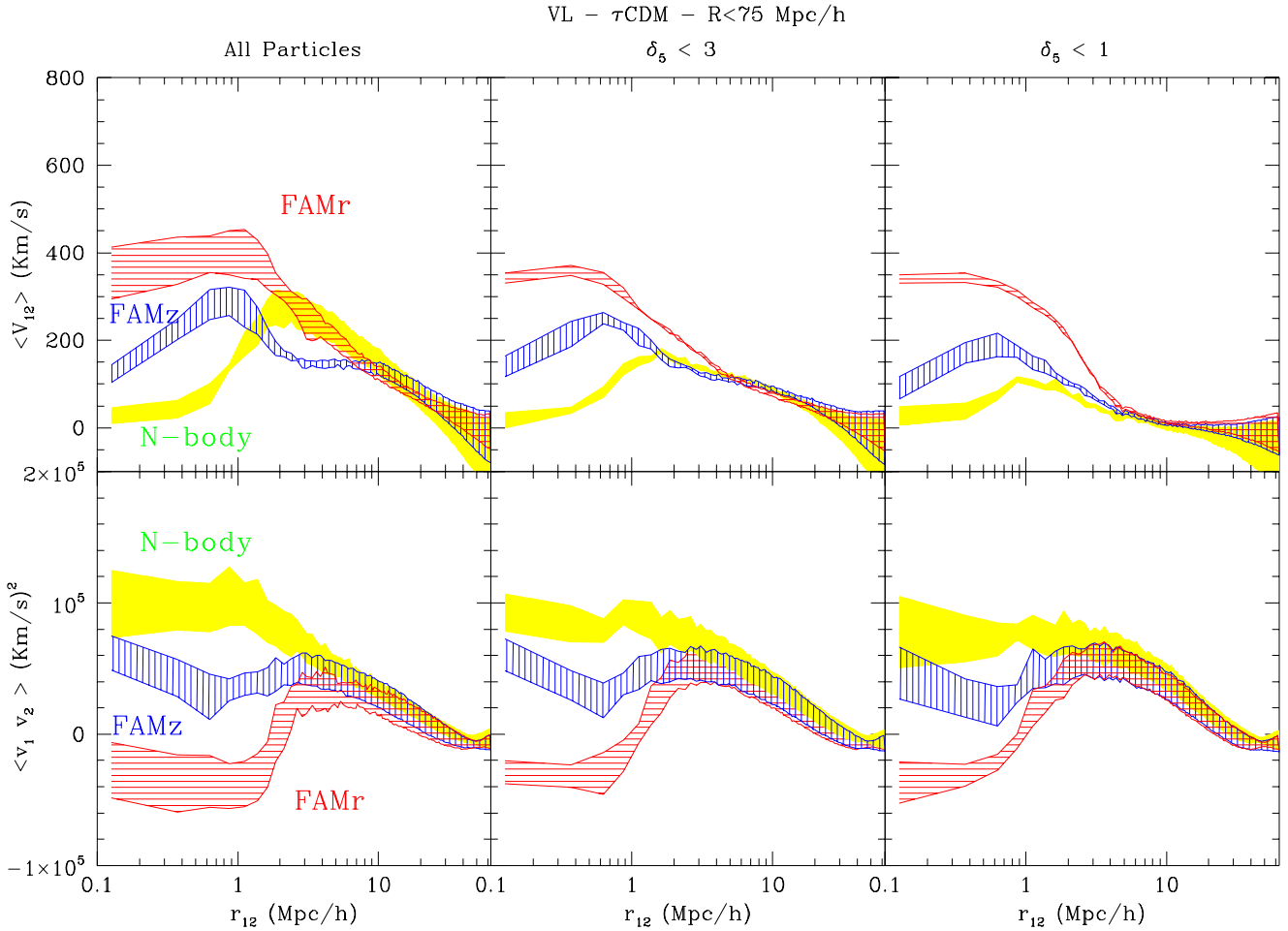


Figure 6. Relative pairwise velocity $\langle V_{12} \rangle$ (upper panels) and velocity correlation function projected along the separation of the pair $\langle V_1 V_2 \rangle$ (lower panels), as a function of the separation r_{12} averaged over the 5 VL- τ CDM catalogs. The “ribbons” represent the 1σ uncertainty intervals around the mean value. Vertically and horizontally-dashed ribbons show the results of the FAMz and FAMr, respectively. The dark strips refer to the N -body experiment. The plots in the central row and those in the row on the right have been obtained by considering points with $\delta_5 < 3$ and $\delta_5 < 1$ and within $75 \text{ h}^{-1} \text{ Mpc}$. All the particles available have been used in the plots on the left.

not necessarily reside in high density environments. For the N -body experiment, however, the strong infall signature around $5 \text{ h}^{-1} \text{ Mpc}$ disappears when neglecting high density regions, meaning that most of the infall signal is contributed by pairs in which at least one member is located in a high density spot.

5.2 Smoothed Volume-Limited: VL5TH

The analysis in Section 5.1 revealed that when high density regions are excluded, FAM predicts an almost unbiased peculiar velocity field and reproduces its correlation properties on scales larger than a few Mpc. Instead of discarding regions where the velocity field is highly non-linear, we can apply FAM on a particle distribution obtained by sampling a smoothed version of the original particle distribution. Clearly, this smoothing operation is rather unrealistic, since real peculiar velocities are too sparse to be smoothed. Thus, the test performed in this Section is ideal. The aim is to minimize “thermal noise” and to concentrate on the effects of sampling errors on FAM velocity prediction. Therefore, here we repeat the analysis of Section 5.1 on the 5TH-smoothed, volume limited mock catalogs VL5TH. However, since the thermal noise has been eliminated by the smoothing procedure, in this section we assume that errors only affect FAM velocity prediction and perform linear regressions of FAM velocities on N -body, with errors on the Y-axis only.

The plots in the central row of fig. 7 show the map of the 5TH-smoothed N -body peculiar velocities interpolated at the particle positions in one of the mock catalogs, for points selected in slices similar to those shown in fig. 4 at the same three different density thresholds. The 5TH-smoothing operation has erased nonlinear signatures such as the virial motions in high

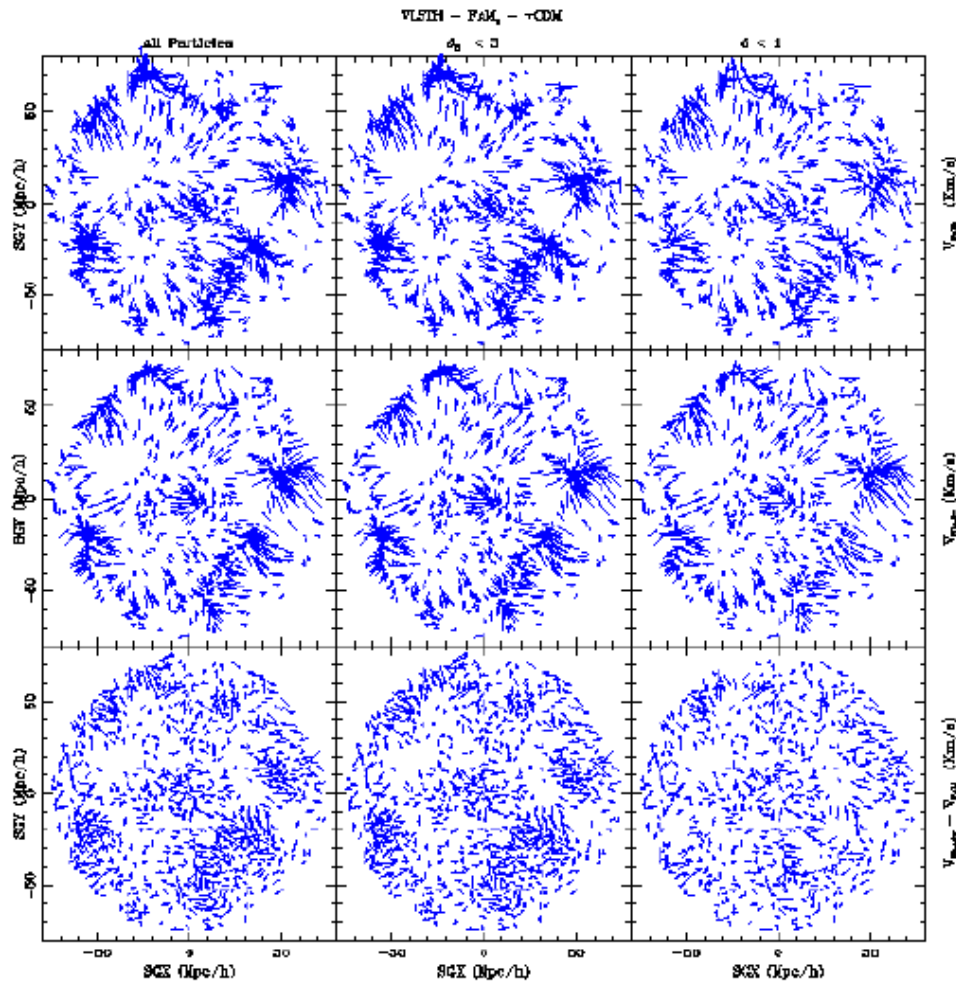


Figure 7. Peculiar velocities in a slice of thickness $6 h^{-1}\text{Mpc}$ cut through one of the VL5TH- τCDM catalogs. Plots in the top row: FAMz velocities. Plots in the middle row: 5TH-smoothed N -body velocities. Plots in the bottom row: velocity residuals $\mathbf{v}_{Nbody} - \mathbf{v}_{FAMz}$. Panels on the left: all the points in the slice are shown. Panels in the middle: points with $\delta_5 < 3$. Panels to the right: points with $\delta_5 < 1$.

density regions. The N -body flow is dominated by large, coherent motions which are well reproduced by FAMz (upper row), as confirmed by the small, incoherent residuals displayed in the plots on the bottom. As expected, none of the results in this Section change when applying different density-cuts. Therefore we will only show and discuss the results relative to the full sample.

The scatter plots in fig. 8 show the v - v comparisons for the 5 VL5TH- τCDM experiments. The parameters of the linear fits are shown in each panel of fig. 8 and listed in table 3. The results of the FAMr experiments are very similar to the FAMz ones and do not depend on the cosmological scenario. In all experiments FAM velocities are slightly larger than the N -body ones. This discrepancy is due to the fact that the softening parameter in use ($\epsilon = 0.5 h^{-1}\text{Mpc}$) is much smaller than the smoothing radius. Increasing the softening to $\epsilon = 3.0 h^{-1}\text{Mpc}$ brings FAM and N -body velocities into agreement, as indicated in table 3. The 1-D velocity scatter around the fit is significantly smaller than the 1-D rms velocity dispersion in the VL5TH catalogs ($\approx 240 \text{ Km s}^{-1}$).

As shown in fig. 9, the analysis of the average relative pairwise velocity (upper panel) and the v - v correlation function (lower panel) demonstrates that the main differences between FAM and N -body velocity fields are on scales smaller than $\sim 5 h^{-1}\text{Mpc}$. Indeed, at small relative separations $\langle V_{12} \rangle_s > \langle V_{12} \rangle_x$ and both are larger than the N -body ones, showing that FAM systematically over-predicts the relative infall velocity. This spurious infall pattern appears because of the small softening $\epsilon = 0.5 h^{-1}\text{Mpc}$. As shown in fig. 10, varying the softening parameter has a large effect on the correlation properties of the FAM velocity field. With a smaller softening of $\epsilon = 0.25 h^{-1}\text{Mpc}$ (horizontally dashed strips) the infall pattern becomes more prominent on small scales. Increasing the softening to $\epsilon = 3.0 h^{-1}\text{Mpc}$ (diagonally dashed strips) reduces spurious infall, and yields correlation properties which are very close to the N -body ones over all scales.

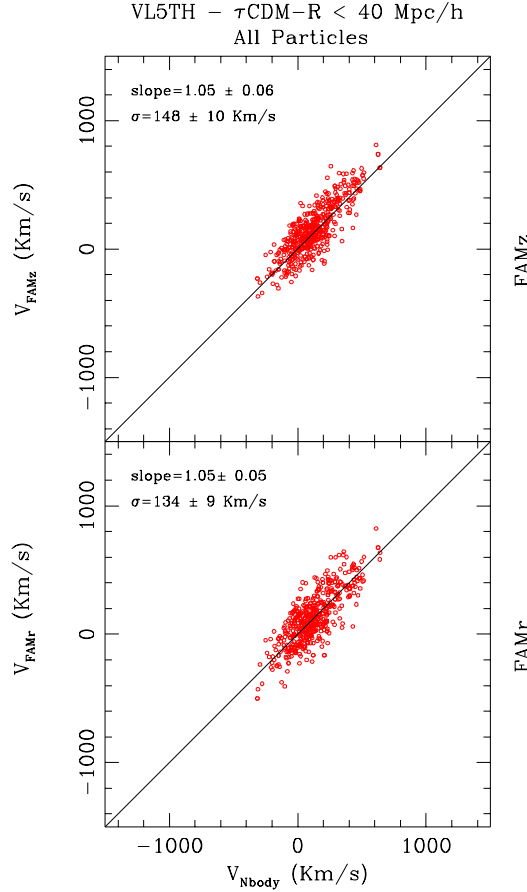


Figure 8. FAM vs. N -body velocity scatter plots in x - (bottom panel) and s -space (top panel) for 500 objects randomly selected from the 5 VL5TH- τ CDM catalogs. The straight line, showing the expected correlation, is plotted to guide the eye. The results of the linear fit are also displayed.

Table 3. FAMr and FAMz results for the VL5TH experiments in the τ CDM (upper part) and Λ CDM (lower part) cosmological models. The average slope, b , and 1-D velocity scatter, σ , along with their rms scatter, are shown for FAM experiments performed with three different value of the softening parameter $\epsilon = 0.25, 0.5, 3 \text{ h}^{-1}\text{Mpc}$.

Model	FAMr			FAMz		
	$\epsilon = 0.25$	$\epsilon = 0.5$	$\epsilon = 3.0$	$\epsilon = 0.25$	$\epsilon = 0.5$	$\epsilon = 3.0$
VL5TH- τ CDM	$b \ 1.07 \pm 0.08$	1.05 ± 0.05	1.08 ± 0.10	1.08 ± 0.09	1.05 ± 0.06	1.02 ± 0.09
	$\sigma \ 154 \pm 22$	134 ± 9	112 ± 8	147 ± 13	148 ± 10	118 ± 8
VL5TH- Λ CDM	$b \ 0.93 \pm 0.06$	1.03 ± 0.05	0.94 ± 0.06	0.93 ± 0.10	1.05 ± 0.06	0.94 ± 0.10
	$\sigma \ 106 \pm 21$	92 ± 3	97 ± 21	115 ± 24	98 ± 6	101 ± 24

5.3 FAMz vs. Linear Theory and PIZA: Volume-Limited case

In this Section we compare the FAMz velocities obtained in the VL experiments of Section 5.1 to those predicted by linear theory and Zel'dovich approximation using the same VL-catalogs. Linear theory predictions have been obtained from the gravity force computed from the particle distribution in s -space at the final time, $\mathbf{g}_{0,i}^s$: $\mathbf{v}_i = H_0 f_0 \mathbf{g}_{0,i}^s$. Note that no attempt is made here to account for s -space distortion effects which could be minimized using iterative procedures (e.g. Yahil *et al.* 1991). Velocities in the Zel'dovich approximation have been obtained by running FAMz with $n_{max} = 1$ basis function which corresponds to straight line orbits $\mathbf{x}_i(D) = H_0^{-1} \mathbf{s}_{i,0} + D \mathbf{C}_{i,1} - f_0 \mathbf{C}_{i,1}^{\parallel} \hat{\mathbf{s}}_{i,0}$. These velocities should be similar to those that would be obtained by applying the PIZA method of Croft & Gaztañaga (1998) in s -space.

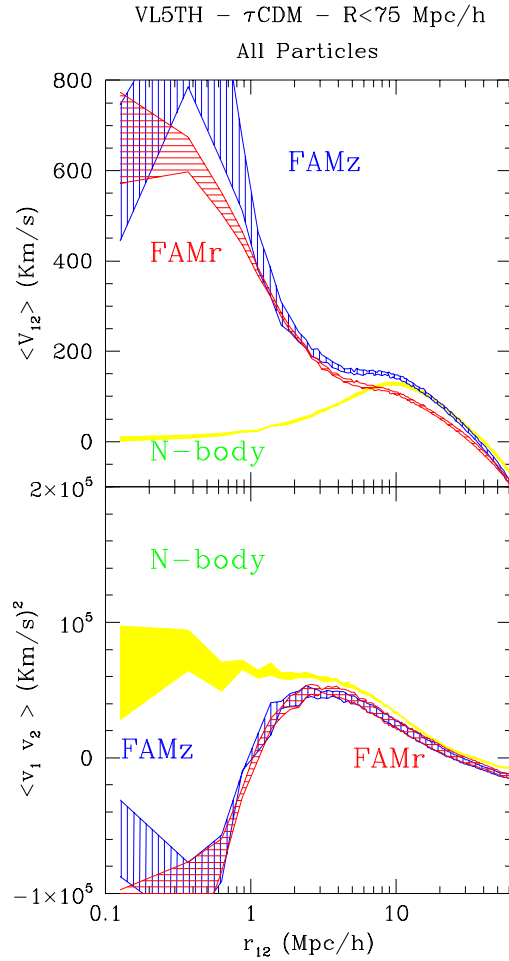


Figure 9. Relative pairwise velocity $\langle V_{12} \rangle$ (upper panel) and velocity correlation function projected along the pair separation, $\langle v_1 v_2 \rangle$ (lower panel), computed from the 5 VL5TH- τ CDM catalogs. The different strips represent 1σ uncertainty intervals around the mean values. Vertically and horizontally-dashed strips refer to FAMz and FAMr experiments, respectively. The dark “ribbon” refers to the N -body case. The correlations are computed using all the particles within $75 \text{ h}^{-1}\text{Mpc}$.

Fig. 11 is similar to fig. 5. The scatter plots in the upper panels show the comparisons between N -body velocities and velocities predicted using linear theory (left), PIZA (middle) and FAMz (right) for 500 objects randomly selected from the 50,000 particles in the 5 VL- τ CDM catalogs.

The scatter plot on the top left panel appears to be dominated by a large number of out-liers which cause linear theory predictions to overestimate peculiar velocities. This is not surprising and derives from sparse sampling, breakdown of linear theory in high density environments and from the fact that s -space distortions were not accounted for. To quantify the mismatch between N -body and linear velocities we have performed a linear regression of N -body velocities on model predictions using all particles in each of the 5 VL- τ CDM catalogs and assuming errors on the Y-axis only. The average slope, 1-D scatter of the regression and their rms values are shown in the panel and listed in table 4 along with the results of the other velocity models. The slope of the best fitting line is very shallow and indicates that linear theory indeed severely overestimates peculiar velocities. The 1-D velocity scatter, however, is rather small compared to the 1-D N -body velocity dispersion ($\approx 350 \text{ Km s}^{-1}$). The situation improves considerably when using either the Zel’dovich approximation (top central) or FAMz (top right). In both cases the slope of the best fitting line increases dramatically, especially for FAMz. The scatter around the fit, instead, remains almost unchanged.

Better results can be obtained by smoothing model velocities on small scales, where all the approximations break down. This is demonstrated by the scatter plots shown in the bottom panels of fig. 11 in which the unsmoothed N -body velocities are compared with peculiar velocities predicted by linear theory (bottom left), PIZA (bottom central) and FAMz (bottom right) all of them smoothed with a Top Hat filter of radius $5 \text{ h}^{-1}\text{Mpc}$. In all cases the match between true and predicted velocities improves considerably, especially for the case of linear theory. However, only FAMz returns unbiased velocity predictions.

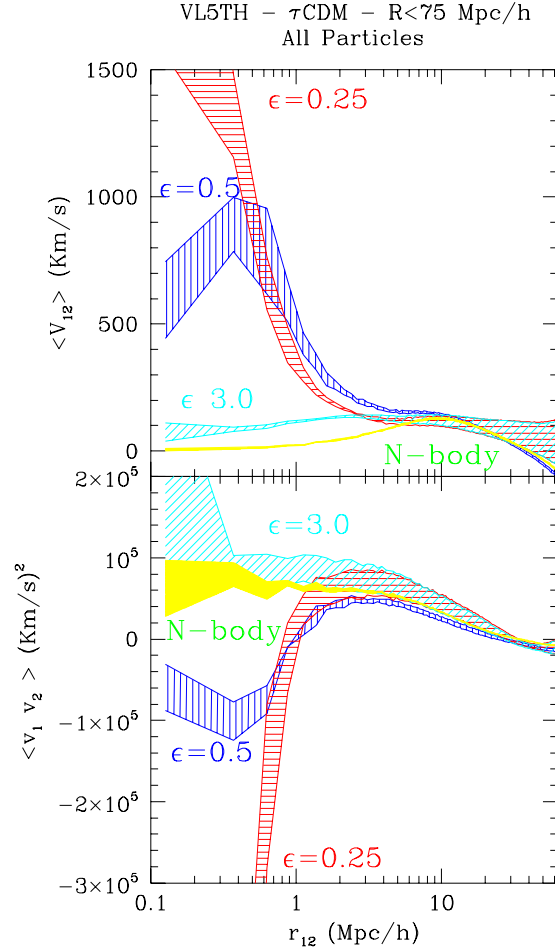


Figure 10. The same functions $\langle V_{12} \rangle$ (upper panel) and $\langle v_1 v_2 \rangle$ (lower panel) displayed in fig. 9 are plotted here for the FAMz case and for three different values of the softening parameter. Horizontally, vertically and diagonally dashed strips refer to $\epsilon = 0.25, 0.5, 3.0 \text{ h}^{-1}\text{Mpc}$, respectively. Note that the scales of the Y-axes are different from fig. 9.

Two sources of errors mainly affect velocity reconstruction methods: sparse sampling and the breakdown of model predictions in the highly nonlinear regime. Both uncertainties affect all velocity-velocity comparisons of fig. 11 (and those in fig. 3 of Nusser & Branchini (2000)), and therefore do not affect the relative comparison of the three reconstruction methods. However, these errors need to be accounted for to estimate absolute errors or when comparing our results with those of other tests that adopt similar velocity models but use different mock catalogs, as in Croft & Gaztañaga (1998) and Berlind, Narayanan & Weinberg (2000). For example, the average inter-particle separation of $4.75 \text{ h}^{-1}\text{Mpc}$ in our mock VL catalogs is similar to the galaxy-galaxy separation in the inner part of redshift catalogs like PSCz, 2dF (Colless *et al.* 2001) and SDSS (Friemann & Szalay 2000) but is larger than that of particles in mock catalogs used to test most velocity models. Furthermore, as explained in Section 4, our mock catalogs contain spurious pairs and triplets of nearby objects. Their presence artificially increases the amplitude of model velocities in high density environments and amplify the magnitude of the reconstruction errors. Both effects conspire in making our error estimates larger than those obtained from more ideal mock catalogs, like those used in the analyses of Croft & Gaztañaga (1998) and Berlind, Narayanan & Weinberg (2000).

To check the dependence of our results on the cosmological model we have repeated the same analysis using the 5 VL- Λ CDM catalogs. The results of the fits to the v - v comparisons are listed in table 4. The performances of PIZA and FAMz in a Λ CDM universe are similar to those obtained in a τ CDM one, indicating that the goodness of the velocity reconstruction depends little on the underlying cosmological model. The failure of linear theory, however, is more severe in the Λ CDM universe. This is a consequence of the fact that this cosmological model is characterized by a larger number of high density peaks in which linear theory breaks down.

Smoothing FAMz velocities with a 5TH filter returns unbiased velocity predictions in both τ CDM and Λ CDM scenarios. Increasing the smoothing length would have the effect of bring PIZA velocities (and, eventually, the linear ones) into agreement

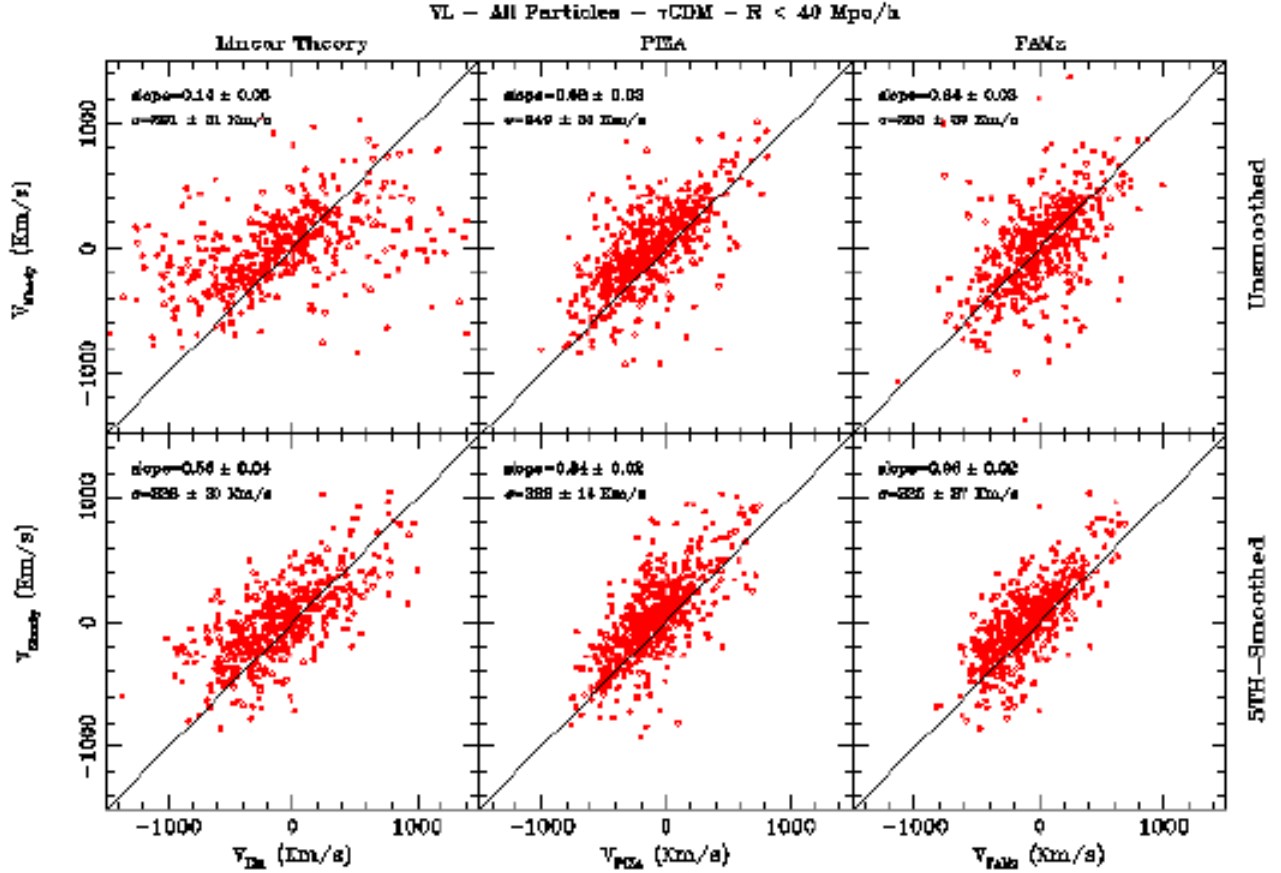


Figure 11. N -body velocities vs. peculiar velocities predicted by linear theory (left), PIZA (middle) and FAMz (right) for ~ 500 objects randomly selected from the 50,000 particles in the VL- τ CDM catalogs. In the upper plots the comparison is performed using unsmoothed peculiar velocities. The predicted velocities in the lower panels have been smoothed with a 5TH filter and are compared with unsmoothed N -body velocities. The results of the fits are shown in all the plots. The straight lines at 45° are drawn to guide the eye.

with the N -body ones. However, as pointed out by, Berlind, Narayanan & Weinberg (2000), increasing the smoothing scale would also cause the FAMz velocity to be underestimated, as a consequence of the fact that errors in predicted velocities correlates with the predicted velocities themselves. We conclude that $5 \text{ h}^{-1}\text{Mpc}$ should be regarded as the optimal smoothing scale for FAMz velocities.

6 TESTS WITH FLUX-LIMITED CATALOGS

Real datasets typically consists of flux (or magnitude) limited catalogs. Here we investigate how well FAM performs when applied to the more realistic mock flux limited catalogs described in Section 4. We will be concerned with flux limited samples and will neglect other possible sources of systematic errors like unobserved regions of the sky (e.g. Zone of Avoidance), the occurrence of morphology and density biases and so on.

In all experiments we have chosen to use the the selection function of PSCz galaxies (eq. 13) since that catalog still represents the deepest all-sky redshift survey presently available. The mass of each mock galaxy is equal to the inverse of the PSCz selection function measured at the galaxy's x -space location. This may generate systematic errors when the FAM reconstruction is performed s -space (i.e. with FAMz) which are included in the error budget in the following two Sections.

Table 4. N -body velocities vs. linear theory, PIZA and FAMz velocity predictions for the VL (upper part) and FL (lower part) experiments and for two different cosmological models (τ CDM and Λ CDM). The average slope, b , and 1-D velocity scatter σ (in Kms^{-1}) are shown along with their rms scatter, measured over all particles in the 5 independent experiments. The best fit values are listed for the case of unsmoothed predicted velocities (left hand side) and 5TH-smoothed predicted velocities (right hand side).

		Unsmoothed			5TH-smoothed		
Model		Linear	PIZA	FAMz	Linear	PIZA	FAMz
VL- τ CDM	b	0.14 ± 0.05	0.58 ± 0.03	0.64 ± 0.03	0.56 ± 0.04	0.84 ± 0.02	0.96 ± 0.02
	σ	291 ± 31	240 ± 30	253 ± 33	238 ± 30	222 ± 14	225 ± 27
VL- Λ CDM	b	0.03 ± 0.02	0.51 ± 0.07	0.58 ± 0.04	0.26 ± 0.04	0.81 ± 0.05	0.98 ± 0.06
	σ	320 ± 50	285 ± 40	295 ± 60	280 ± 57	254 ± 35	271 ± 56
FL- τ CDM	b	0.13 ± 0.02	0.52 ± 0.07	0.74 ± 0.04	0.65 ± 0.05	0.93 ± 0.04	1.03 ± 0.04
	σ	291 ± 23	249 ± 25	242 ± 16	232 ± 18	223 ± 11	213 ± 9
FL- Λ CDM	b	0.04 ± 0.01	0.47 ± 0.06	0.57 ± 0.06	0.28 ± 0.06	0.88 ± 0.04	1.01 ± 0.04
	σ	270 ± 60	210 ± 26	232 ± 31	223 ± 52	192 ± 28	209 ± 23

6.1 Unsmoothed Flux-Limited: FL

We have applied FAMz to the unsmoothed, flux limited catalogs labeled FL in table 1 and displayed in the upper-right panel of fig. 3. In this Section we present the results of v - v analyses analogous to those in Section 5.1.

The v - v scatter plots for FL- τ CDM catalogs are shown in fig. 12, both for FAMz (upper panels) and FAMr (lower panels), for three different overdensity cuts. The scatter plots look similar to those of the volume limited tests (fig. 5). The parameters of the linear regression of N -body velocities on FAM which are listed in the lower part of table 2 confirm the visual impression that FAM velocities are systematically larger than the N -body ones. Moreover, FAMr produces systematically larger velocities than FAMz. The mismatch and between FAM and N -body velocities decreases outside high density environments. For $\delta_5 < 1$, FAMr and FAMz velocities are only 10–20% larger than the N -body ones and the mismatch further decreases when performing the 4σ clipping procedure described in Section 5.1. The analogy with the results found in is Section 5.1 shows that selection effects do not seem to affect FAM performances too much. The most striking feature is perhaps that the scatter around the fit is very similar to that found in the volume limited experiment of Section 5.1. FAM performances are similar in the τ CDM and Λ CDM cosmological models despite of their very different values of σ_8 , and greatly improve when high density environments are excluded from the analysis.

Also the results of the velocity correlation analysis are quite similar to those of the unsmoothed-volume limited tests, as it is evident from the similarities between figs. 6 and 13. However, selection effects are responsible for three main differences. First, the amplitude of the difference between FAM and N -body velocity correlations below $\sim 1 \text{ h}^{-1}\text{Mpc}$ is twice larger than in the volume-limited case. Second, the agreement with the N -body results shifts to a somewhat larger scale. Third, the scatter around the mean correlation value increases.

The results of this Section show that, when applied to mock PSCz flux-limited catalogs, FAMz produces almost unbiased estimates of peculiar velocities outside high density regions. Moreover, the correlation properties of the FAM and N -body velocity fields agree on scales larger than $5 - 8 \text{ h}^{-1}\text{Mpc}$. These results are remarkably close to those of the volume-limited tests.

6.2 Smoothed Flux-Limited: FL5TH

In the previous sub-section we have applied FAM to the particle distribution in the FL catalogs. Here we perform an ideal experiment analogous to that of Section 5.2 and show the results of FAM applied to the FL5TH catalogs in which the objects sample a smoothed version of the particle distribution in the FL catalogs. A typical FL5TH mock catalog is displayed in the bottom-right panel of fig. 3. As for the case of the VL5TH tests discussed in Section. 5.2, the results do not depend on the local density and therefore we only show the results relative to the full sample.

Fig. 14 shows the v - v comparison for the 5 FL5TH- τ CDM experiments. As in Section. 5.2 we have performed linear regressions of FAM velocities on N -body ones, where errors are associated to FAM velocities only. The results are displayed in fig. 14 and in table 5. They show that FAM peculiar velocities are systematically smaller than the N -body ones. Such

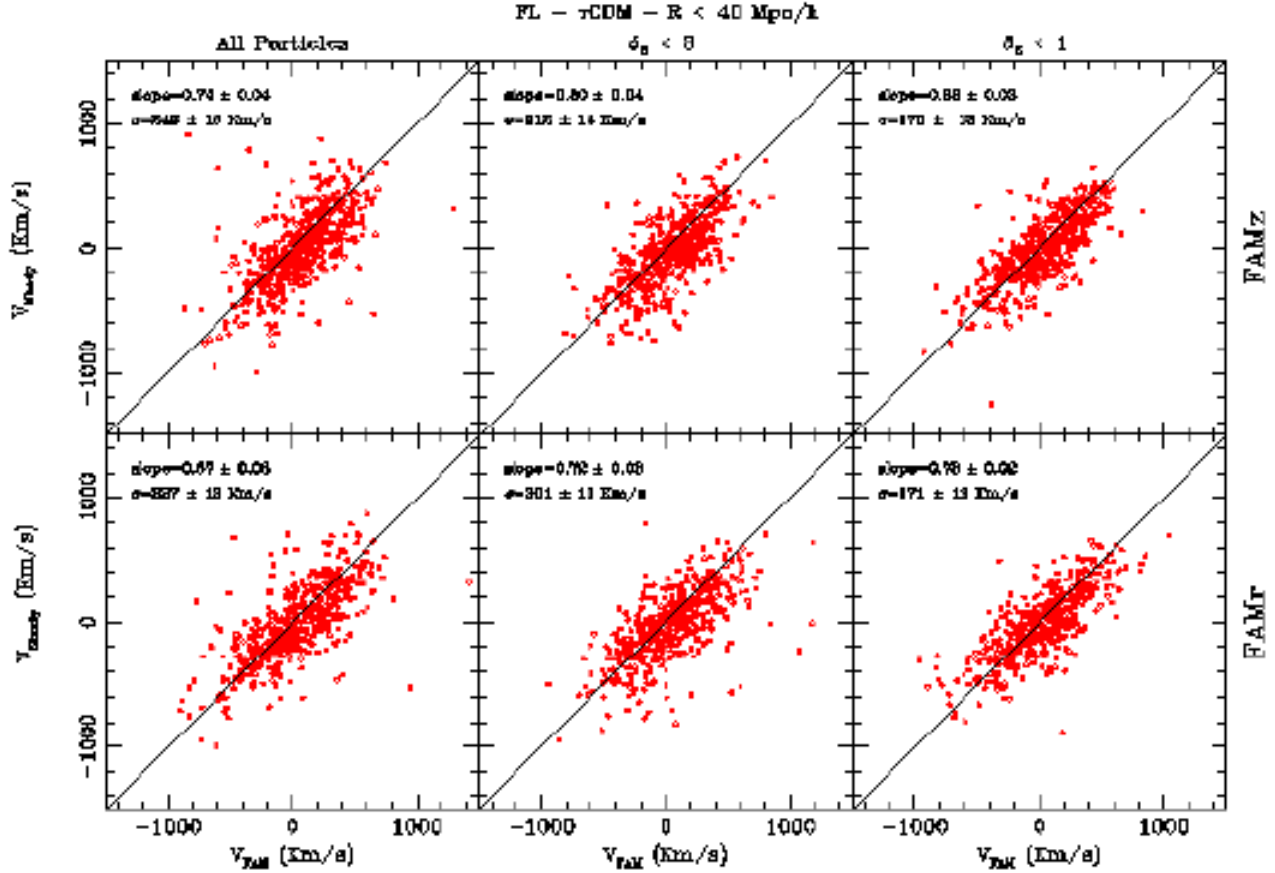


Figure 12. N -body vs. FAM velocity scatter plots in x - (bottom panel) and s -space (top panel) for 500 randomly selected objects from the 5 FL- τ CDM catalogs. Panels on the left: all particles. Panels in the middle: particles with $\delta_5 < 3$. Panels on the right: particles with $\delta_5 < 1$. The straight line shows the expected correlation. The results of the fit are shown in all the panels.

Table 5. FAMr and FAMz results for FL5TH experiments in the τ CDM (upper part) and Λ CDM (lower part) cosmological models. The average slope, b , and 1-D velocity scatter, σ (in Km s^{-1}), measured over the 5 independent experiments are shown along with their rms scatter.

	FAMr	FAMz
Model	All	All
FL5TH- τ CDM	b 0.93 ± 0.10	0.91 ± 0.11
	σ 174 ± 17	288 ± 75
FL5TH- Λ CDM	b 0.93 ± 0.07	0.99 ± 0.20
	σ 142 ± 27	256 ± 134

discrepancy, however, is below the 1σ significance level. The random errors are larger than in all previous tests, especially for the FAMz method, probably indicating that the smoothing-resampling procedure enhances the amplitude of the shot noise errors. It is important to stress that, like in the VL5TH tests, the results do not change when applying different density cuts, which indicates that by applying the smoothing-resampling strategy there is no need of identifying high density environments and exclude them from the v - v analyses. FAMr results seem to depend little on the underlying cosmological model, as indicated by the results listed in the lower part of table 5. This is not true for FAMz, indicating that in a universe with a large value of σ_8 , characterized by the presence of many high density peaks, some of them enhanced by effect of the shot noise and smeared by s -space distortions, the smoothing-resampling procedure might not be sufficient in providing FAMz-velocity predictions which are uniform throughout the volume of the sample.

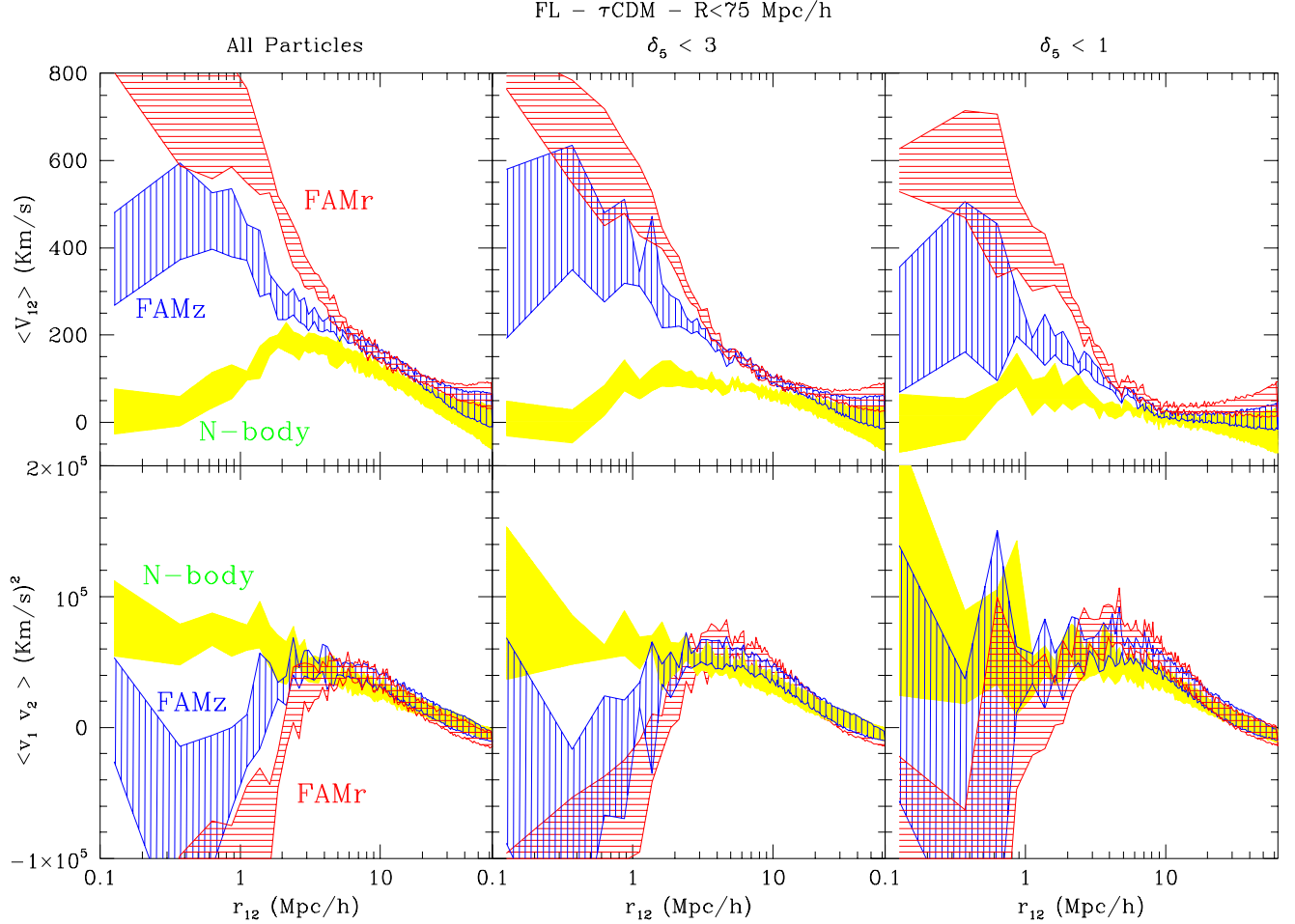


Figure 13. $\langle V_{12} \rangle$ (upper panels), and $\langle v_1 v_2 \rangle$ (lower panels), as a function of the pair separation r_{12} from 5 FL- τ CDM experiments. Vertically-dashed strip: FAMz. Horizontally-dashed strip: FAMr. Dark strip: N-body. Left panels: all the particles are considered. Central panels: particles with $\delta_5 < 3$. Right panels: particles with $\delta_5 < 1$.

The effect of shot-noise is particularly dramatic for FAM velocity correlations. As seen in fig. 15, the random uncertainties in the predicted velocity correlations become extremely large below the scale of $\sim 2 h^{-1}$ Mpc. On scales larger than $2 h^{-1}$ Mpc the results look similar to those obtained from the flux limited tests, displayed in the plots on the left hand side of fig. 12. In particular, the 1σ uncertainty strip of the FAM-predicted $\langle V_{12} \rangle$ statistics overlaps with the N-body result on scales larger than $\sim 8 h^{-1}$ Mpc. A similar behavior also characterizes the $\langle v_1 v_2 \rangle$ statistics. In this case, however, the agreement between FAM and N-body is already found down to scales as small as $\sim 3 h^{-1}$ Mpc.

6.3 FAMz vs. Linear Theory and PIZA: Flux-Limited case

In this section we repeat the analysis performed in Section 5.3 and compare the FAMz velocities discussed in Section 6.1 with those predicted by linear theory and PIZA in s-space, using the same FL catalogs.

The results for the 5 FL- τ CDM catalogs are displayed in fig. 16 which is analogous to fig. 11 and show the v - v comparison between unsmoothed N-body velocities and velocities predicted by linear theory (top left), PIZA (top central) and FAMz (top right). Predicted velocities in the lower panels were smoothed using a Top Hat filter with an adaptive radius $R_{TH} = \text{Max}[5, l] h^{-1}$ Mpc, where l is the average particle-particle separation at the given redshift. The results of the linear regressions of N-body velocities on the predicted ones are displayed in fig. 16 and in the lower part of table 4.

When no smoothing is applied to predicted velocities (upper panels), all methods overestimate the peculiar velocities. The situation is thus similar to that of the volume limited experiment performed in Section 5.3. This bias is particularly severe in the case of linear theory and decreases significantly by applying a top hat smoothing of radius $R_{TH} \simeq 5 h^{-1}$ Mpc to predicted velocities, as shown by the scatter plots in the bottom panels. In particular, FAMz smoothed velocity predictions

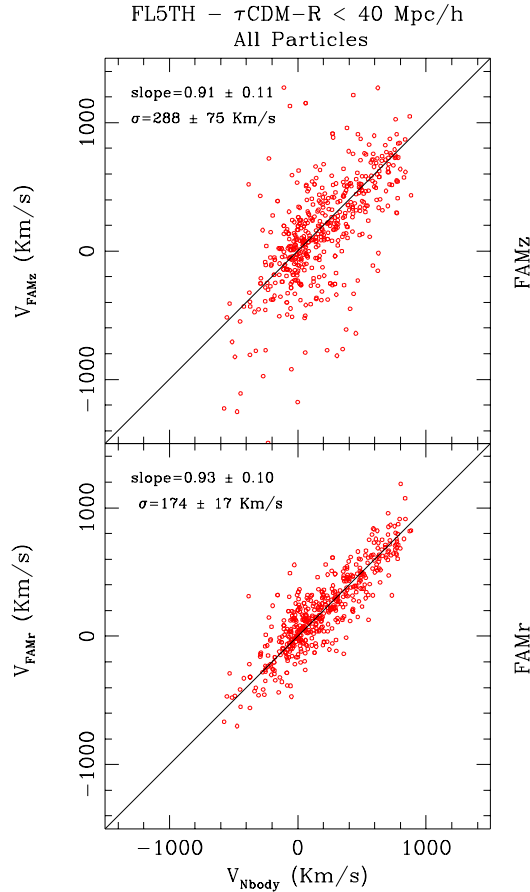


Figure 14. Same as fig. 8 but referring to the 5 FL5TH- τ CDM mock catalogs.

are bias-free and with a random error of of 220 Kms^{-1} , nearly independent on the underlying cosmological model. These results demonstrate that, unlike the two other method considered here, applying FAMz to a PSCz-like redshift catalog allow to predict a model for the cosmic velocity field which is unbiased, provided that FAMz velocities are smoothed on a scale of $\sim 5 \text{ h}^{-1}\text{Mpc}$.

7 SUMMARY AND CONCLUSIONS

We presented extensive tests of the FAM method for reconstructing peculiar velocities from particle distribution in x- and s-space. Using the analytic spherical collapse model and a suite of realistic volume-limited and flux-limited mock catalogs, we showed that FAM can successfully recover peculiar velocities from the particle distribution in x- and s-space. Errors in the predicted velocities are mainly due to shot noise and highly nonlinear motions that FAM fails to model correctly. Shot noise errors depend on the sparseness of galaxy sampling and thus on the particular dataset considered. To obtain a realistic error estimate we set the number density of galaxies in our mock catalogs similar to that in the inner part of the real PSCz, 2dF and SDSS catalogs. Errors due to nonlinear motions can be reduced by avoiding high density regions. Indeed, discarding objects in the highest density peaks brings systematic errors down to a level smaller than 20% and reduces the amplitude of random uncertainties from $\sim 250 \text{ Kms}^{-1}$ to $\sim 150 \text{ Kms}^{-1}$ in the volume limited experiments. When applied to flux-limited mock catalogs mimicking the distribution of galaxies in the PSCz redshift survey, FAM systematic errors outside dense regions are still below 20 % and the 1-D random velocity errors amount to $120 - 170 \text{ Kms}^{-1}$. Moreover, FAM recovers the correlation properties of the underlying velocity field down to scales of $\sim 5 \text{ h}^{-1}\text{Mpc}$ in both flux and volume limited cases. In practice, it may be difficult to measure the local density from sparse datasets, in order to discard high density peaks. However, particles in these regions have very large velocity residuals, and appear as out-liers in the v - v scatter plots. Eliminating all points deviating by more than 4σ from the best fitting line improves the results of the fit and returns velocity estimates which are almost

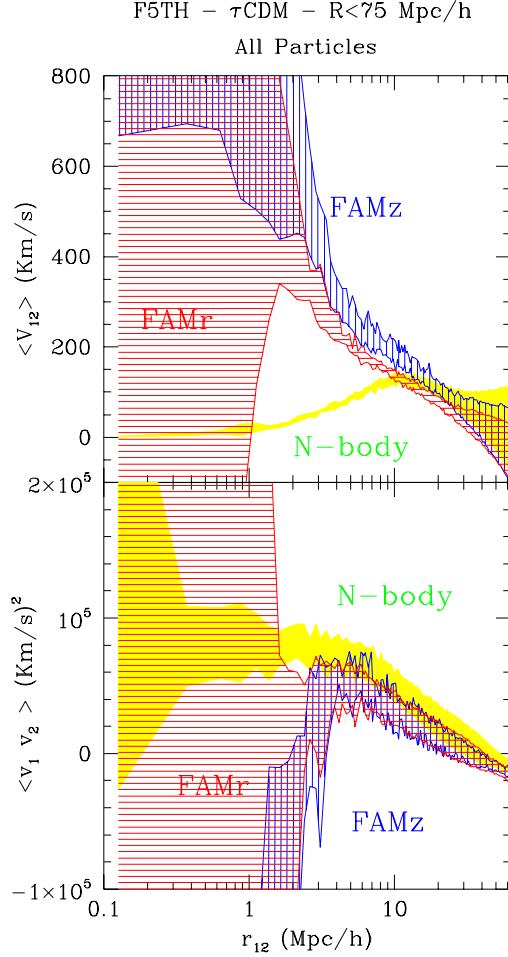


Figure 15. Same as fig. 9 for the case of 5 FL5TH- τ CDM experiments.

unbiased. Another strategy to reduce the impact of nonlinear motions is that of smoothing the model velocity field. We have found that FAMz velocities smoothed with a Top Hat filter of radius $5 h^{-1} \text{Mpc}$ are free of systematic biases. Clearly, there is nothing fundamental in this smoothing scale. To the contrary, the amount of smoothing required to minimize systematic errors depends on the strength of nonlinear motions, sampling rate and on the particular method used to compare model and observations. Other reconstruction methods like those based on linear theory and Zel’dovich approximation could also predict unbiased velocities, provided that an appropriate smoothing filter is applied. However, the smoothing scale required by FAMz to eliminate systematic errors is smaller than that required by linear theory or PIZA and thus allow to retain more information which lead to a more precise estimates of cosmological parameters such as $\beta = \Omega_m^{0.6}/b$.

Since FAM errors depend on several external factors, like the particular dataset considered, it is difficult to compare our results with those of other analyses. For example, it is somewhat surprising that errors in the Cartesian components of FAMz velocities predicted from our mock PSCz catalogs are a factor of two larger than those of the velocities obtained by applying the the iterative, quasi-linear model of Sigad *et al.* (1998) to the IRAS 1.2 Jy. catalog (see Willick *et al.* 1997). Indeed, the better treatment of nonlinear dynamics by FAMz and the denser sampling of the PSCz catalog should reduce these uncertainties rather than increase them. As discussed by Branchini *et al.* (2001), this apparent inconsistency derives from the differences in the mock catalogs used to calibrate the two reconstruction methods. Peculiar velocities in our mock catalogs, extracted from the AP³M simulations of Cole *et al.* (1998), are more nonlinear than those of the mock catalogs used Willick *et al.* (1997) that were extracted from PM *N*-body simulations. The higher “temperature” of the velocity field in our mocks increases the uncertainties in the velocity reconstruction procedure. Errors in velocity predictions are further amplified by the spurious pairs and triplets of nearby particles contained in our mocks. The net result is that our estimated FAMz velocity errors are larger that those of Willick *et al.* (1997). Another example is given by the large systematic errors affecting our linear velocity predictions compared to FAM velocities, as shown by figures 16 and 11. This result suggests that estimates of β from $v - v$ comparisons that use a linear model velocity field based on the PSCz catalog (e.g. Nusser *et al.* (2000) and Branchini *et al.* (2001)) are biased low and that this bias could be reduced by using the FAMz model, instead.

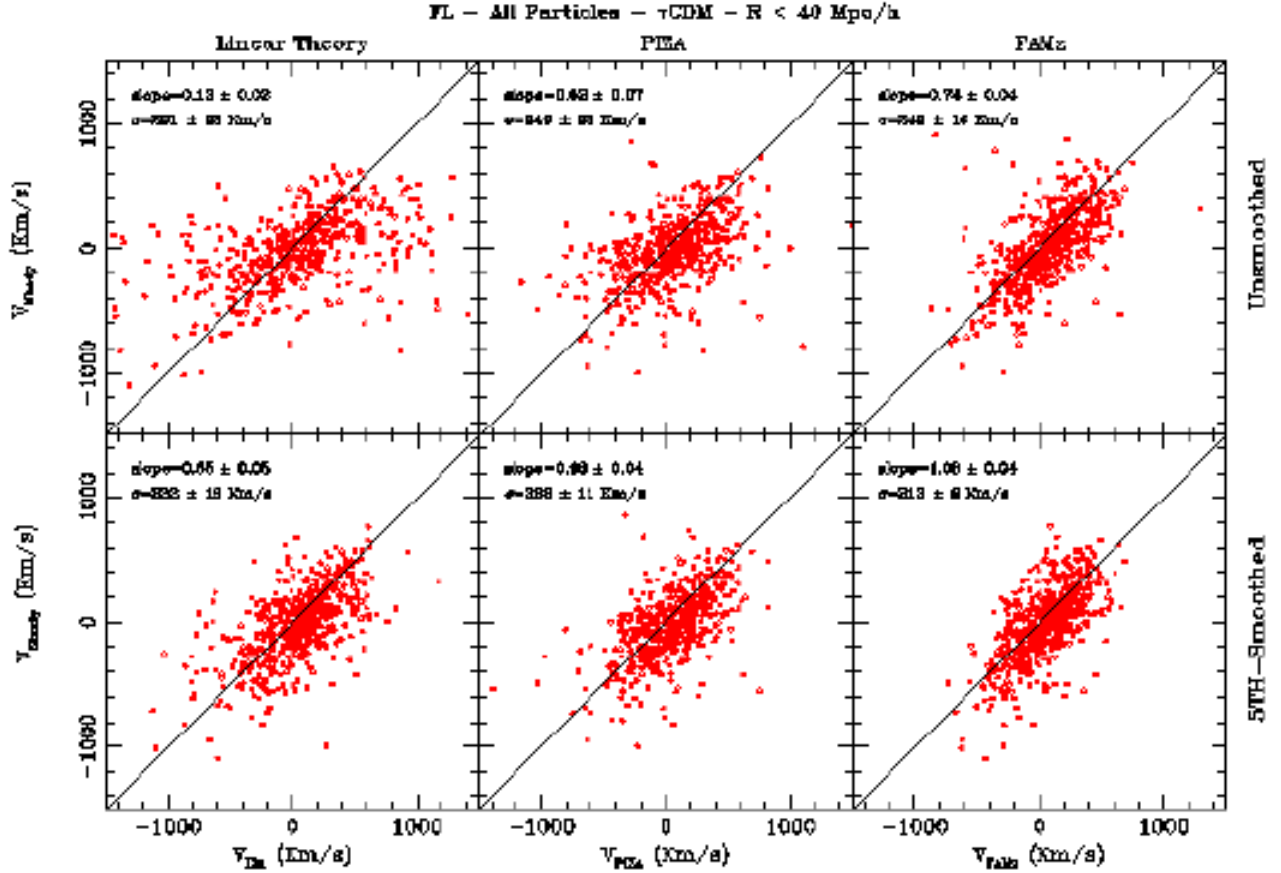


Figure 16. Same as fig. 11 for the case of FL- τ CDM catalogs.

A quantitative assessment of this bias and its reduction, however, needs to account for the differences between the various models and analyses. First of all the linear model used by Nusser *et al.* (2000) and Branchini *et al.* (2001) was corrected for redshift s-space distortions while our model is not. Second, in this work the $v - v$ comparisons are performed through simple linear regressions while the VELMOD analysis of Branchini *et al.* (2001) and the mode-by-mode comparison of Nusser *et al.* (2000) are less trivial and require additional manipulation of the data that may affect the estimate of β . While we plan to quantify these effects in a future paper we also point out that the tests performed by Branchini *et al.* (2001) and Nusser *et al.* (2000) have indicated that possible systematic errors on β are below the 20 % level. The two previous examples illustrate that the results presented in this work are only valid for volume limited and flux limited samples that mimic the PSCz catalog. As for any reconstruction method, random and systematic errors need to be estimated again when a new dataset is considered or a new model vs. data analysis is implemented. Such error analysis is best done by applying FAM to a set of realistic mock catalogs, as we did in this work

The dependence of the clustering properties on the type of real galaxies implies that most galaxies are biased tracers of the underlying mass fluctuations (Loveday *et al.* 1995, Baker *et al.* 1998, Hawkins *et al.* 2001, Norberg *et al.* 2001). NB have shown that a local biasing scheme can be easily incorporated in FAM by assigning to each particle a mass proportional to $\mathcal{W} = (1 + \delta)/(1 + \delta^g)$ where δ and δ^g are, respectively, the mass and galaxy density contrast in the vicinity of the particle. Alternatively, given \mathcal{W} one can obtain the mass density field from the galaxy distribution. The mass density field can then be sampled by a discrete particle distribution to be used as input in FAM, instead of the original biased particle distribution. Any biasing relation is naturally defined in real space; hence an application of FAM on a distribution of galaxies in s-space must be done iteratively, if biasing is to be incorporated properly. Nevertheless, several authors have shown that forcing a biasing relation in s-space does not introduce large errors (e.g. Verde *et al.* 1998, Scoccimarro *et al.* 2001, Szapudi 1998, Sigad, Branchini & Dekel 2000, Narayanan *et al.* 2001). By making reasonable assumptions on the statistical properties of the mass density, it is even possible to derive the biasing relation in redshift space directly from the redshift catalog. For example, a biasing scheme can be obtained by mapping the probability distribution function (PDF) obtained from the galaxy

distribution into a mass PDF which is assumed to be log-normal (Sigad, Branchini & Dekel 2000) or by extensively applying hybrid reconstruction techniques (e.g. Narayanan *et al.* 2001). In future work, we will test FAM using different biasing schemes and also using mock galaxy catalogs extracted from “galaxies” identified in N -body simulations using semi-analytic models (e.g., Kauffmann, Nusser & Steinmetz 1997, Kauffmann *et al.* 1999, Benson *et al.* 2000).

Methods based on the least action principle, like FAM, can serve as a time machine for recovering the particle positions and velocities at any early epoch. The particle distribution can then be filtered to obtain the density field as a function of time. A backward reconstruction of the large scale structure can be very rewarding. It can provide an estimate for the initial density field and this could discriminate among different cosmological scenarios, e.g. by detecting non-Gaussian features in the primordial density field or by measuring its power spectrum (Nusser, Dekel, & Yahil 1995, Kolatt *et al.* 1996, Monaco *et al.* 2000, Narayanan *et al.* 2001). The performance of FAM as a time machine has only been tested on the scale of the Local Group in real space with no biasing (Peebles 1990, 1994), or with a simple halo biasing prescription (Dunn & Laflamme 1993, Branchini & Carlberg 1994). Therefore, there is a need for thorough testing of FAM to establish its reliability at recovering the past orbits in redshift space, over scales of cosmological interests and using realistic, time-dependent biasing schemes (Nusser & Davis 1994, Fry 1996, Matarrese *et al.* 1997). While we plan to address these issues in a future paper it is important to note that our results, along with those obtained by NB, show that FAMz performs better than linear theory and PIZA (Croft & Gaztañaga 1998) in reconstructing peculiar velocities at the present epoch. It is therefore reasonable to expect that the FAMz will also improve over PIZA backward reconstruction and thus will be able to recover the correct initial conditions down to scales smaller than $\sim 3 h^{-1}\text{Mpc}$, without enforcing any *prior* power spectrum like in the Perturbative Least Action procedure (Goldberg & Spergel 2000).

The results of our tests indicate that, once applied to the PSCz catalog, FAMz will be able to model the cosmic velocity field down to scales of a few Megaparsecs with 1-D random uncertainty of $150 - 200 \text{ Km s}^{-1}$, hence improving over presently available models also obtained from the PSCz catalog using either linear theory (Branchini *et al.* 1999) or the PIZA method (Valentine, Saunders & Taylor 2000). We plan to use this new velocity model to perform $v - v$ comparisons that should return an estimate of $\Omega_{m,0}$, with an expected 1σ uncertainty of $10 - 15\%$ and, because of the wide range of scales probed by the recent data, to provide valuable information on the scale dependence of the biasing relation.

In this paper, FAM has been applied to systems containing up to $N = 2 \cdot 10^4$ particles. Since the computational cost of FAM reconstructions scales as $N \log N$, the method can also be applied to new generation redshift surveys containing 10^5 to 10^6 objects, like the 2dF and SDSS catalogs. In these new catalogs, however, the surveyed regions span only a fraction of the celestial sphere. This constitutes a potential problem for reconstruction methods like FAM which require to be applied to spherical catalogs to minimize the dynamical influence of the neglected mass distributed outside the volume of the sample. A possible way to proceed is to reconstruct the velocity field over a series of spherical sub-catalogs carved out of the parent survey. The sampling within these sub-catalogs will be denser than in the PSCz catalog and the velocity model less affected by shot noise. As a result, applying the FAMz procedure to a set of spherical sub-samples filling the volume of the parent catalog would return an unbiased model velocity fields on unprecedented large scales and with 1-D random uncertainties of about 100 Km s^{-1} . This would lead to a precise determination of the distribution of mass which could then be cross-correlated with absorption features in AGN spectra either due to the intervening cold, neutral hydrogen ($\text{Ly}\alpha$ line) or to the warm-hot intergalactic medium (O_{VI} and O_{VII} lines) to determine the ill-known baryon fraction at $z=0$. Another possibility would be to compare FAM velocity prediction with precise velocity measurements of galaxies in the very local universe, like those obtained from the Surface Brightness Fluctuation method (Tonry *et al.* 2000, 2001). This should allow to measure the value of $\Omega_{m,0}$ with an even higher precision.

8 ACKNOWLEDGMENTS

EB thanks the Technion of Haifa for its hospitality while part of this work was done. AN acknowledges the support of a grant from the Norman and Helen Asher Space Research Institute. This research is supported by the Technion V.P.R Fund-Henri Gutwirth Promotion of Research Fund, and the German Israeli Foundation for Scientific Research and Development.

REFERENCES

- Baker J.E., Davis M., Strauss M.A., Lahav O., Santiago B.X., 1998, ApJ, 508, 6
 Benson A.J., Cole S., Frenk C.S., Baugh C.M., Lacey C.G., 2000, MNRAS, 311, 793
 Berlind A.A., Narayanan V.K., Weinberg D.H., 2000, ApJ, 537, 537

- Bertshinger E., Dekel, A., 1989, ApJ, 335, L5
 Bouchet F.R., Hernquist L., 1988, ApJS, 68, 521
 Branchini E., Carlberg, R.G., 1994, ApJ, 434, 37
 Branchini E., Teodoro L., Frenk C.S., Schmoltdt I., Efstathiou G., White S.D.M., Saunders W., Sutherland W., Rowan-Robinson M., Keeble O., Tadros H., Maddox S., Oliver S., 1999, 308, 1
 Branchini E., Freudling W., Da Costa L. N., Frenk C. S., Giovanelli R., Haynes M. P., Salzer J. J., Wegner G., Zehavi I., 2001, MNRAS, 326, 1191
 Cole S., Hatton S., Weinberg D., Frenk C.S., 1998, MNRAS, 300, 945
 Colles M., and The 2dFGRS Team, 2001, astro-ph/0106498
 Croft R.A.C., Gaztañaga E., 1998, ApJ, 495, 554
 Davis M., Nusser A., Willick J.A., 1996, ApJ, 473, 22
 Dunn A.M., Laffamme R. 1993, MNRAS, 264, 865
 Eke V.R., Cole S., Frenk C.S., MNRAS, 282, 263
 Frieman J. A., Szalay A. S., 2000, Phys. Reports, 333, 215
 Frisch, U., Matarrese S., Mohayaee R., Sobolevski A., astro-ph/0109483
 Fry J.N., 1996, ApJ, 461, L65
 Giavalisco M., Mancinelli P.J., Yahil A., 1993, ApJ, 411, 9
 Goldberg D.M., Spergel D.N., 2001, ApJ, 544, 21
 Goldberg D.M., 2001, ApJ, 552, 413
 Gorski K., 1988, ApJ, 332, 7
 Gramann M., 1993, ApJ, 405, 449
 Hawkins E., Maddox S., Branchini E., Saunders W., 2001, MNRAS, 325
 Kauffmann G., Nusser A., Steinmetz M., 1997, MNRAS, 286, 759
 Kauffmann G., Colberg J.M., Diaferio A., White S.D.M., 1999, MNRAS, 307, 537
 Kolatt T., Dekel A., Ganon G., Willick J., 1996, ApJ, 457, 460
 Loveday J., Maddox S.J., Efstathiou G., Peterson B.A., 1995, ApJ, 442, 457
 Mancinelli J.P., Yahil A., 1995, ApJ, 452, 75
 Matarrese S., Coles P., Lucchin F., Moscardini L., 1997, MNRAS, 286, 115
 Monaco P., Efstathiou G., 1999, MNRAS, 308, 763
 Monaco P., Efstathiou G., Maddox S.J., Branchini E., Frenk C.S., McMahon R.G., Oliver S.J., Rowan-Robinson M., Saunders W., Sutherland W.J., Tadros H., White S. D. M., 2000, MNRAS, 318, 681
 Narayanan V.K., Weinberg D.H., 1998, ApJ, 508, 440
 Narayanan V.K., Croft R.A.C., 1999, ApJ, 523, 328
 Narayanan V.K., Weinberg D.H., Branchini E., Frenk C.S., Maddox S., Oliver S., Rowan-Robinson M., Saunders W., 2001, ApJS, 136, 1
 Norberg P., and The 2dFGRS Team, 2001, astro-ph/0105500
 Nusser A., Dekel A., 1992, ApJ, 391, 443
 Nusser A., Davis M., 1994, ApJ, 421, L1
 Nusser A., Dekel A., Yahil A., 1995, ApJ, 449, 439
 Nusser A., Colberg J.M., 1998, MNRAS, 294, 425
 Nusser A., Branchini E., 2000, MNRAS, 313, 587
 Nusser A., da Costa L., Branchini Enzo., Bernardi M., Alonso M., Wegner Gary., Willmer C., Pellegrini P., 2000, MNRAS, 320, L21
 Peebles P.J.E., 1980 *“The Large Scale Structure in The Universe”*, Princeton University Press, Princeton.
 Peebles P.J.E., 1989, ApJ, 344, L53
 Peebles P.J.E., 1990, ApJ, 362, 1
 Peebles P.J.E., 1994, ApJ, 429, 43
 Phelps S. 2000, *“New Applications of the Action Principle in Cosmology”*, Ph.D. Thesis, Princeton University
 Press W.H., Teukolsky S.A., Vetterling W.T., Flannery B.P., 1992, *“Numerical Recipes”*, Cambridge University Press, Cambridge
 Saunders W., 1996, PSCz web site: <http://www-astro.physics.ox.ac.uk/~wjs/pscz.html>
 Saunders W., Sutherland W.J., Maddox S.J., Keeble O., Oliver S.J., Rowan-Robinson M., McMahon R.G., Efstathiou G.P., Tadros H., White S.D.M., Frenk C.S., Carraminana A., Hawkins M.R.S., 2000, MNRAS, 317, 55
 Santiago B.X., Strauss M.A., Lahav O., Davis M., Dressler A., Huchra J.P., 1995, ApJ, 446, 457
 Santiago B.X., Strauss M.A., Lahav O., Davis M., Dressler A., Huchra J.P., 1996, ApJ, 461, 38
 Schmoltdt I., Saha P., 1998, AJ, 115, 223
 Scoccimarro R., Feldman H.A., Fry J.N., Frieman J.A., 2001, ApJ, 546, 652
 Shaya E.J., Peebles P.J.E., Tully R.B., 1995, 454, 15
 Sharpe J., Rowan-Robinson M., Canavezes A., Saunders W., Branchini E., Efstathiou G., Frenk C., Keeble O., McMahon R.G., Maddox S., Oliver S.J., Sutherland W., Tadros H., White S.D.M., 2001, MNRAS, 322, 121
 Sigad Y., Eldar A., Dekel A., Strauss M., Yahil A. 1998, ApJ, 495, 516
 Sigad Y., Branchini E., Dekel A., 2000, ApJ, 540, 62
 Strauss, M.A., Ostriker J.P., Cen R., 1998, ApJ, 494, 20
 Susperregi M., 2001, ApJ, 546, 85
 Szapudi I., 1998, MNRAS, 300, 35
 Tonry J.L., Blakeslee J.P., Ajhar E.A., Dressler A., 2000, ApJ, 530, 625
 Tonry J.L., Dressler A., Blakeslee J.P., Ajhar E.A., Fletcher A.B., Luppino, G.A., Metzger M.R., Moore C.B., 2001, ApJ, 546, 681
 Valentine H., Saunders Will., Taylor A., 2000, MNRAS, 319, 13
 Verde L., Heavens A.F., Matarrese S., Moscardini, L., 1998, MNRAS, 300, 747
 Whiting A.B., 2000, ApJ, 533, 50
 Willick, J., Strauss, M., Dekel, A., Kolatt, T. 1997b, ApJ, 486, 629

Willick, J., Strauss, M. 1998, ApJ, 486, 629

Yahil A., Strauss M.A., Davis M., Huchra J.P., 1991, ApJ,372, 380

Zaroubi S., Hoffman Y., Fisher K., Lahav O., 1995, ApJ, 449, 446

Zel'dovich Y.B., 1970 A&A 5, 84

This figure "Fig1.gif" is available in "gif" format from:

<http://arxiv.org/ps/astro-ph/0110618v3>

This figure "Fig2.gif" is available in "gif" format from:

<http://arxiv.org/ps/astro-ph/0110618v3>

This figure "Fig3.gif" is available in "gif" format from:

<http://arxiv.org/ps/astro-ph/0110618v3>

This figure "Fig4.gif" is available in "gif" format from:

<http://arxiv.org/ps/astro-ph/0110618v3>

This figure "Fig5.gif" is available in "gif" format from:

<http://arxiv.org/ps/astro-ph/0110618v3>

This figure "Fig7.gif" is available in "gif" format from:

<http://arxiv.org/ps/astro-ph/0110618v3>

This figure "Fig11.gif" is available in "gif" format from:

<http://arxiv.org/ps/astro-ph/0110618v3>

This figure "Fig12.gif" is available in "gif" format from:

<http://arxiv.org/ps/astro-ph/0110618v3>

This figure "Fig16.gif" is available in "gif" format from:

<http://arxiv.org/ps/astro-ph/0110618v3>